International Journal of Mechanical Sciences 213 (2022) 106865

Contents lists available at ScienceDirect

International Journal of Mechanical Sciences

journal homepage: www.elsevier.com/locate/ijmecsci

Coupling between inherent and machining-induced residual stresses in aluminum components

Ritin Mathews [a], Sumair Sunny [a], Arif Malik [a,*], Jeremiah Halley [b]

[a] Department of Mechanical Engineering, The University of Texas at Dallas, Richardson TX 75080, USA
[b] Tech Manufacturing, LLC, 45 Cooperative Way, Wright City, Missouri 63390, USA

ARTICLE INFO

Keywords:
Residual stress
Stress reconstruction
Distortion
High-speed machining
Wrought aluminum alloys
High aspect-ratio parts

ABSTRACT

This work investigates the coupling of inherent residual stress (IRS) and machining-induced residual stress (MIRS) on the final-state of residual stress (FRS) and distortion when high-speed machining (HSM) high aspect-ratio aluminum components. Motivation for this work stems from the simplifications in related numerical investigations that give rise to two limitations: First, the mapping of incompatible, incomplete, and/or spatially scarce IRS profiles generates unrealistic distortions and incorrect stress fields during static equilibration. Second, the simulation of machining via element deletion, inactive elements approach, or Boolean subtraction (removal) of material either ignores thermal and MIRS effects, or implements them based on simplified analytical/empirical models. Such practices therefore prevent a thorough understanding of how IRS and MIRS are coupled. Accordingly, two wrought aluminum 7050 blocks having different IRS profiles (based on stress relief) are considered in this work. An iterative stress reconstruction algorithm is implemented to numerically model a spatially-complete and fully-compatible IRS field in each aluminum block using limited data from slitting measurements documented in the literature. A 2D orthogonal cutting model is used to validate the material and damage models employed, as well as to elucidate the influences of IRS and MIRS on FRS. A 3D end milling model, which adopts the validated material and damage definitions, is then applied with different tool paths to reveal the coupled effects of IRS and MIRS on the distortion when HSM a C-channel featuring high aspect-ratio walls. The results reveal that the interaction between IRS and MIRS is nonlinear in nature, thus contrasting assumptions allowing for their superposition, as are widely reported and adopted in the literature. The results also show that the nonlinear coupling between IRS and MIRS varies according to both the component and location of stress within the machined part. Moreover, the findings reveal that the final part distortion is significantly influenced by the nonlinear coupling, as well as the specific machine tool path implemented.

1. Introduction

Aluminum alloys are highly sought after in the aerospace and automotive industries given their relatively high strength to weight ratio and effortless machinability [1]. 7000 series aluminum alloys, manufactured through rolling and quenching processes, are favored by the aerospace industry in particular, due to their high strength, toughness, and corrosion resistance [2]. Unfortunately, the rolling and quenching processes give rise to residual stress (RS) within the bulk material that cannot be relieved via heat treatment without some compromise in the desired qualities. Methods like stretch-stress relief, which uniaxially stretch the material to plastic strains of 1.5 to 3%, can help reduce the magnitude of the RS, although they do not eliminate it entirely [3]. As a result of RS within the bulk material, monolithic components made from wrought aluminum, and featuring sections having high aspect-ratios, i.e., ratio of height to thickness, may be susceptible to undesired distortion or "warpage" that arises during high-speed machining (HSM) [4,5]. Hence, there exists considerable demand for researching the physics of the machining process so as to capture the influence of RS, especially in aluminum alloys, in order to mitigate distortion and satisfy tighter tolerances [6].

HSM has been a topic of interest to researchers for over four decades. Even before its proliferation in industry, studies on HSM revealed its promise in improving tool life and its significant capability for producing high-quality, machined monolithic components [18]. Pre-existing RS within the wrought material, prior to machining, known as

---

* Corresponding author.
E-mail address: Arif.Malik@utdallas.edu (A. Malik).

https://doi.org/10.1016/j.ijmecsci.2021.106865
Received 18 July 2021; Received in revised form 12 September 2021; Accepted 4 October 2021

Table 1
Summary of the numerical and experimental studies on inherent residual stress and distortion that emerges when machining wrought aluminum.

Author (Year)	Summary of research, key findings, and modeling simplifications relevant to the present work
Guo et al. (2009) [7]	• Numerically investigated machining-induced distortion in high aspect-ratio aerospace components fabricated from Al 7075-T7351. • Used a modified layer-removal method to measure IRS in the wrought specimen. • The rolling and transverse stress components were averaged at different depths through the thickness of the rolled plate, and subsequently introduced into the FE model. • Imposed IRS on final undeformed geometry, to observe distortion. • 18% difference between the numerically predicted and experimentally measured distortion; Suggested due to the neglection of temperature.
Chatelain et al. (2011) [8]	• Experimentally investigated machining-induced distortion in thin-walled Al 7475-T7351 components. • Two Al specimens featuring different stress-relief processes were used as wrought material to obtain variations between their respective IRS profiles. • IRS and FRS were characterized using neutron diffraction (ND), while distortion was measured using a CMM. • IRS in the wrought material was found to influence final part distortion.
Huang et al. (2013) [9]	• Experimentally investigated the influence of machining parameters on MIRS in wrought Al 7050-T7451 specimens. • MIRS was measured using X-ray diffraction (XRD) technique. In-depth RS was determined by removing material layer by layer, using electropolishing method, accompanied by XRD measurements, up to a depth of 100 μm. • Analysis of variance technique was utilized to determine the influence of machining parameters on MIRS. • Variations in MIRS resulting from variations in parameters were attributed to the machining forces and thermal effects.
Richter-Trummer et al. (2013) [10]	• Experimentally and numerically investigated the post-machining distortion generated in an Al 7075-T73 high aspect-ratio component. • Distortion in the experiment was measured via CMM. • Rolling and transverse components of IRS in the bulk material were measured using layer removal method. • Part distortion prediction was obtained by superimposing the IRS profile onto the final geometry. • Predicted distortion in the longitudinal direction was significantly higher than the experimental measurement.
Huang et al. (2015) [11]	• Experimentally and numerically investigated the machining-induced distortion in an Al 7050-T7451 monolithic thin-walled component. • Milling operation by end milling to include MIRS and chemical milling to avoid MIRS were performed. • MIRS measurement was performed using XRD and electro-polishing technology. • Part distortion was measured by a 3D CMM. • IRS was measured using crack compliance method. • Numerical prediction of distortion was obtained by: (1) Superimposing IRS onto the final geometry, and (2) Superimposing IRS onto the final geometry and introducing MIRS on near surface elements by linear superposition. • A maximum error of 26.2% was observed between the experimental and predicted distortions. • About 90% of the total distortion was attributed to IRS and the remaining 10% was attributed to MIRS. • Superposition of IRS and MIRS was predicted to aggravate distortion.
Cerutti and Mocellin (2016) [12]	• Experimentally and numerically investigated the part distortion in an Al 2050-T84 monolithic thin-walled component. • Distortion in the part post-machining was determined via a CMM. • Layer removal method was used to measure rolling and transverse components of IRS. • Boolean deletion technique was used to numerically predict the post-machining distortion due to IRS. • Distortion suffered by the part was observed to be larger during the early stages of machining. • Results reveal that tool path design needs to account for IRS in the bulk material.
Becker (2016) [13]	• Computationally investigated the post-machining part distortion in an Al 7050-T7451 monolithic thin-walled component. • Rolling and transverse components of IRS were measured via slitting method. • The measured IRS was mapped onto the final undeformed part geometry to predict distortion generated due to IRS. • Distortion predicted reveals that IRS in the bulk material has minimal impact on the final part distortion.
Ma et al. (2019) [14]	• Experimentally and computationally investigated the post-machining part distortion in an Al 7050-T7451 thin-walled component considering the influence of IRS and MIRS. • Part distortion observed in the experiment was measured using a CMM. • Rolling and transverse components of IRS in the bulk material were measured using the slitting method for subsequent modeling. • Rough machining operation was modeled using element deletion approach and a simplified analytical model was used to model MIRS during machining. • Modeling without MIRS features a direct map of IRS onto the wrought block before element deletion sequence. • Modeling with MIRS features a technique where elements on the cut surface are assigned MIRS and internal elements are assigned IRS to predict the final part distortion. • The model with MIRS predicted distortion with an error of 17% whereas the model without MIRS predicted distortion with an error of 37% compared to experimentally determined distortion. • Results indicate that redistribution of IRS is the underlying cause of distortion in thin-walled components, however, MIRS should not be neglected.
Barcenas et al. (2020) [15]	• Experimentally and numerically investigated the part distortion in an Al 7050-T7451 monolithic thin-walled component. • Experimental measurement of distortion was performed using a 3D scanner. • Measurement of IRS profile in the rolling and transverse directions were performed by a modified layer removal method. • Homogeneous map of IRS on the wrought block was performed to model IRS. • Element deletion approach was used to model the machining process. • Results show that part positioning inside the wrought block has an influence on the final part distortion.
Casuso et al. (2020) [16]	• Experimentally and numerically investigated post-machining part distortion in an Al 7075-T7651 component. • Experimental distortion was measured using a CMM. • IRS measurement was performed via a modified hole drilling method at multiple locations on the wrought block. • Thermomechanical effects of cutting process were not considered.

(*continued on next page*)

Table 1 (*continued*)

Author (Year)	Summary of research, key findings, and modeling simplifications relevant to the present work
	• An order of magnitude difference in the measured and predicted distortions was observed. • Inaccuracy was speculated to be due to misrepresentation of IRS.
Fan et al. (2020) [17]	• Investigated the post-machining part distortion in Al 6061-T651 monolithic components based on energy principle. • The influence of clamping, cutting loads, and MIRS were ignored. • IRS measured via crack compliance technique. • Experimental and numerical prediction of distortion were performed. • Distortion in the experiment was measured using a CMM. • Element deletion technique was utilized for numerical prediction. • A maximum error of 26.5% was observed between the distortion predicted via energy principle and experiment. • Increase in fluctuation of IRS within the bulk material resulted in greater distortion.

"inherent residual stress" (IRS) can influence distortion in machined parts [19,20]. Stresses that arise during the machining processes, known as "machining-induced residual stress" (MIRS), can also influence distortion in machined parts. MIRS depends on a combination of numerous factors including cutting edge radius, clearance angle, and tool wear, among other machining process parameters [21]. Analytical models attempting to capture the mechanics of the machining process, within the spectrum of simple static to complex dynamic models, were developed during the early stages of HSM [22]. Computational models to study the stress, distortion, cutting forces, temperature, and chip formation in machining were introduced in the early 1970s and have been evolving ever since [22]. Computational frameworks to build predictive models for machining generally involve either Lagrangian or Eulerian formulations. Lagrangian models, where the mesh moves along with the material, are advantageous when it comes to modeling solid mechanics problems, but they cannot be used in cases of excessive/extreme deformations. Techniques like node splitting and remeshing can help overcome this issue, but they increase computational cost [23]. In Eulerian models, on the other hand, the material is tracked within a fixed reference mesh, enabling continuous flow of material around the tool without necessitating node splitting or remeshing. The Eulerian method is computationally more efficient than the Lagrangian method but is not suited for intermittent machining or discontinuous chip formation [23]. Experiments investigating the influence of machining process parameters on the distribution of RS and distortion in high aspect-ratio components provide a means to benchmark predictions from numerical approaches [24,25]. A summary of relevant numerical and experimental studies into IRS and distortion that emerge when machining wrought aluminum is provided in Table 1.

From Table 1, two limitations arise due to simplifications made in the numerical models:

(1) The inherent residual stress within the wrought specimens to be machined was not comprehensively spatially mapped and, additionally, certain components of IRS were omitted (or assumed to be zero). Thus, a balanced and compatible state of stress was not implemented as an initial condition in the simulations. During the simulation, equilibration via strain-displacement generates unrealistic distortions and incorrect stress and strain fields. Regions within the wrought material where strain measurements were not performed would either have zero stress or the same stress as the measured regions depending on the stress mapping technique [7,10–17]. Note, to the authors knowledge, there are no investigations to date that map a full, spatially encompassing, balanced and compatible IRS field in the wrought aluminum specimen prior to simulating HSM.
(2) Even if a full spatial map of the IRS were included, simulating machining via element deletion, inactive elements approach, or Boolean subtraction (removal) of material either completely ignores thermal and MIRS effects, or implements them based on simplified analytical or empirical models [7,10,12–17]. This inhibits achieving a thorough understanding of how IRS and MIRS are coupled.

These shortcomings provide motivation for the three hypotheses tested in this work:

(1) It is hypothesized that final-state of residual stress (FRS) in machined aluminum components is influenced by IRS, but the degree of influence of IRS on the corresponding FRS varies based on both the magnitude and distribution of the IRS profile.
(2) It is hypothesized that there exists a coupling effect between IRS and MIRS that influences final part distortion in high aspect-ratio components machined from wrought aluminum.
(3) It is hypothesized that tool path influences this coupling between IRS and MIRS such that any potential reduction in distortion achievable through choice of tool path is greater than that achievable via reduction in IRS magnitude.

This work aims to investigate the nature of interaction between IRS and MIRS, that must be accounted for during mathematical optimization of process parameters including tool path strategy. Accordingly, two wrought Al 7050 blocks (or specimens) featuring different IRS profiles are modeled herein and subsequently machined into a high aspect-ratio C-channel to test the aforementioned hypotheses. Section 2 of this paper describes how two IRS profiles measured using the slitting method are reconstructed in an FE model of the wrought aluminum blocks. Following this, Section 3 describes the material constitutive (flow stress) and damage models implemented. In addition, Section 3 also discusses a 2D orthogonal cutting model used to validate the Al 7050 material and damage models, as well as a 3D end-milling model wherein the C-channel is machined using two different tool paths from the wrought aluminum blocks featuring the different IRS profiles. A comparison of the FRS, resulting from two IRS profiles is presented in Section 4. Furthermore, the distortion in the high aspect-ratio C-channel is also presented and examined in Section 4 to elucidate whether or not a coupling does indeed exist between IRS and MIRS. Finally, a summary of the key findings from investigating potential coupled effect of IRS and

MIRS on FRS and distortion in high aspect-ratio aluminum components is presented in Section 5.

2. Reconstruction of the inherent residual stress field for a wrought aluminum block

In this work, the IRS in two different grades of a wrought aluminum block, determined by Prime and Hill [3], is reconstructed in a 3D Lagrangian finite element (FE) model to examine the influence IRS has on the FRS, i.e., post-machining RS. It should be noted that the demonstrated modeling approach is extensible to other geometries and materials as well.

2.1. Overview of residual stress measurements obtained via slitting method

Prime and Hill [3] used the slitting method, depicted in Fig. 1 (*Left*), to measure and analyze the IRS in blocks of aluminum alloys 7050-T74 (without stretch stress relief) and 7050-T7451 (with stretch stress relief). The slitting method uses wire electrical discharge machining (wire EDM) to introduce a planar slit in a metallic block containing IRS via incremental cuts through the depth in a particular direction. As the incremental cuts are made, IRS is released on the slit face and the resulting deformation is measured as a function of the incremental slit depth by a strain gage adhesively mounted near the entry point of the wire into the block (front gage), as well as another strain gage mounted on the opposite face of the block (back gage). RS components existing normal to the slit plane, prior to the wire EDM cuts, can subsequently be computed from the measured strains [26]. Note, the slitting method assumes that each stress component measured at every incremental cut is averaged along the length of the slit at that depth. Prime and Hills measurements revealed a difference in the IRS magnitude and distribution through the depth (mutually perpendicular to the rolling and transverse directions) of the wrought aluminum blocks, when comparing the two grades, as presented in Fig. 1 (*Center and Right*). The limited data on stress components, i.e., only the rolling and transverse direction components, necessitates stress reconstruction, discussed next, to obtain a fully compatible state of stress over the entire block prior to executing the high-speed machining (HSM) models.

2.2. Iterative stress reconstruction algorithm

A challenge with numerical modeling of IRS is that the experimental measurement data is typically incomplete, either in terms of stress components or limited/scarce measurement locations across an entire wrought specimen. Destructive testing techniques such as slitting, or contour methods can be used to measure RS over larger regions but are limited to one or two components of stress per test [26]. Once a specimen is tested, it is permanently altered from its original form and further measurements cannot be used without making suitable assumptions. Non-destructive testing techniques such as X-ray and neutron diffraction can measure all the components of stress but are limited to small regions in the order of 10 to $10^3 \mu\text{m}$ [27]. Numerical solutions such as inverse eigenstrain method [28–30], Airy stress function approach [31–35], and the iterative stress reconstruction algorithm (ISRA) [36–38] have been sought to overcome the challenge of reconstructing a fully compatible stress field from limited experiment data. While the inverse eigenstrain and Airy stress function approaches would benefit from a priori knowledge of the eigenstrain distribution within the rolled aluminum blocks, these approaches would also require implementing a great number of basis functions considering the large dimensions (100 mm × 100 mm × 75 mm) of the wrought aluminum blocks used in the demonstrated investigation [39]. ISRA works well even in the absence of full spatial coverage of experimental measurements, and/or limited stress component data [40]. Hence, ISRA, as illustrated by Fig. 2, is implemented herein to reconstruct the IRS prior to executing the 3D HSM models.

Once the location and magnitude of IRS components has been determined experimentally, a Lagrangian, static-equilibration, linear-displacement based FE model is built to replicate the volume of the aluminum blocks. The initial IRS is set to zero, ubiquitously ($\boldsymbol{\sigma}_{\text{ij}}^0 = 0$). Elements, $\mathbf{E}^m$, are identified in locations of the FE model representative of positions within the aluminum block where slitting measurements were made and are overwritten with the experimentally determined IRS components, $\boldsymbol{\sigma}_{\text{ij}}^m = 0$. The first equilibration iteration ($k = 1$) of ISRA is

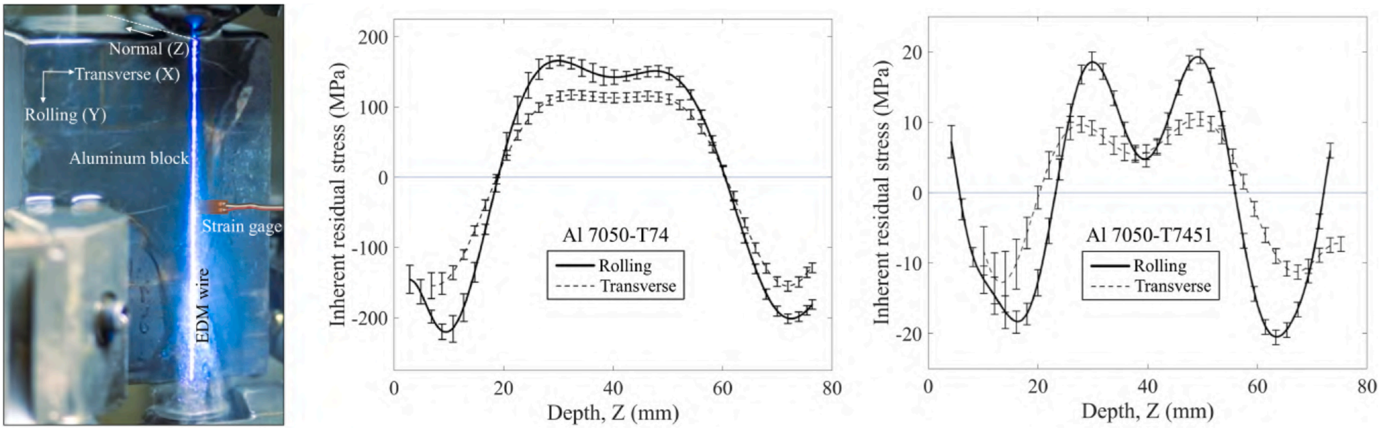

Fig. 1. (*Left*) Photograph of the slitting method. (*Center* and *Right*) Inherent residual stress (IRS) profiles adapted from slitting measurements by [3] for wrought Al 7050-T74 (without stretch stress relief) and Al 7050-T7451 (with stretch stress relief) blocks, respectively. Note, the IRS magnitude range and spatial distribution differs considerably comparing both grades of aluminum as a result of stretch stress relief.

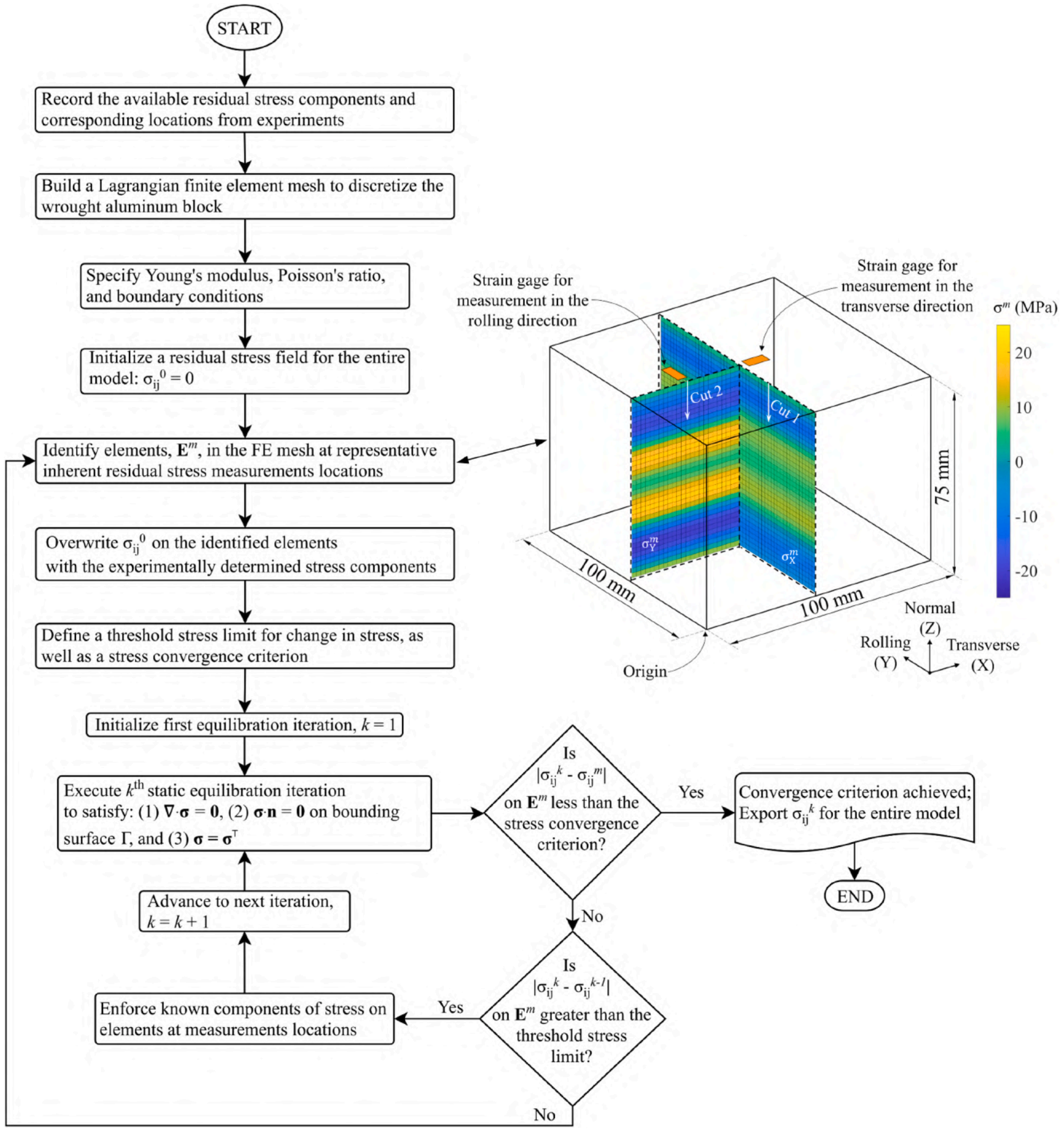

Fig. 2. Overview of the iterative stress reconstruction algorithm (ISRA).

then executed to satisfy stress equilibrium conditions given by Eqs. (1) and (3):

$$\nabla\cdot\boldsymbol{\sigma} = \mathbf{0} \tag{1}$$

$$\boldsymbol{\sigma}\cdot\mathrm{n} = \mathbf{0}, \text{ on surface } \boldsymbol{\Gamma} \tag{2}$$

$$\boldsymbol{\sigma} = \boldsymbol{\sigma}^{\mathsf{T}} \tag{3}$$

where, $\boldsymbol{\sigma}$ is the symmetric Cauchy stress tensor which can be expressed as seen in Eq. (4), in terms of the material stiffness tensor, $\mathbf{C}$, the elastic strain tensor, $\boldsymbol{\varepsilon}$, and $\mathbf{n}$ is the unit outward normal vector to the surface, $\boldsymbol{\Gamma}$, that bounds the volume of the aluminum block.

$$\boldsymbol{\sigma} = \mathbf{C} : \boldsymbol{\varepsilon} \tag{4}$$

Once equilibrium is achieved, the stresses, $\boldsymbol{\sigma}_{ij}^k$, at measurement locations, $\mathbf{E}^m$, are subject to two convergence criteria: (1) The first criterion verifies if the stress components have converged, i.e., it checks if the absolute difference between $\boldsymbol{\sigma}_{ij}^k$ and $\boldsymbol{\sigma}_{ij}^m$ at $\mathbf{E}^m$ is less than a predefined convergence limit. In this work, the stress convergence limit is set to 100 kPa which is less than 25% of the average experimental measurement error. (2) A threshold stress criterion serves the purpose of continuing the ISRA search process only when the change in stress between iterations is of sufficient magnitude (to prevent an infinite loop when convergence is not obtained). The threshold stress limit is set to 10 kPa herein (one order of magnitude less than the stress convergence limit). The iterative process is implemented using a Python script and the final reconstructed, $\boldsymbol{\sigma}_{\mathrm{ij}}^{k}$, represents a compatible, spatially distributed stress field.

For computational efficacy, the aluminum block is discretized using linear hexahedral elements with a uniform mesh size of ~2 mm. For ISRA, only the Youngs modulus, 71.016 GPa, and Poissons ratio, 0.33, at room temperature are implemented in the material definition [41]. The algorithm has active translational and rotational degrees of freedom, and solutions to Eqs. (1),(2),(3),(4) are computed with the implicit solver of Abaqus v6.14. ISRA is implemented for both grades of wrought aluminum tested by Prime and Hill [3], i.e., T74 (without stretch stress relief) and T7451 (with stretch stress relief). The corresponding reconstructed stress fields are compared with the experimentally determined stress components along the rolling and transverse directions, as a function of depth (Z), as shown in Fig. 3. The faint lines illustrate the variation of the rolling and transverse stress components, over k iterations, as they approach convergence. Note, the reconstructed field also includes the remaining components of the symmetric stress tensor, albeit the challenge of non-uniqueness of the compatible reconstructed $\boldsymbol{\sigma}_{\mathrm{ij}}^{k}$ can arise when implementing ISRA due to limited experimental measurement data; In locations where measurements were not made, a compatible stress field is still obtained, however, it may not necessarily reflect the actual stress field in that location of the block. The use of limited data from Prime and Hill [3] is still justified considering that the primary goal is to study the influence of the IRS on HSM, rather than rigorous prediction of the IRS within the aluminum block. The reconstructed IRS is implemented as an initial state in the HSM model, described next.

3. High-speed machining models

To simulate the RS and distortion that result from the machining process and investigate the influence of IRS, 2D and 3D cases of machining performed on the aluminum blocks are modeled. The 2D orthogonal cutting model, presented later in Section 3.2, features a highly refined mesh and helps validate the material model and damage criteria. The material and damage definitions are implemented in the 3D end-milling model presented later in Section 3.3. The mesh described in Section 2 is adopted for the 3D cases, however, the elements used in both the 2D and 3D models now feature temperature and displacement degrees of freedom. Material removal is implemented via element deletion featuring an energy-based exponential damage evolution. Thermophysical material properties for aluminum 7050 are applied in conjunction with a Johnson-Cook (J-C) flow stress definition [42] as well as ductile and shear damage models, described next.

3.1. Material model and damage criteria

Thermophysical material properties such as density, Young's modulus, Poisson's ratio, thermal conductivity, thermal expansion coefficient, and specific heat are referenced from [2,41,43]. The temperature and strain-rate sensitive flow stress, σ_f, is governed by the J-C plasticity model, given by Eqs. (5) and (6), which has been found to be well suited for high strain-rate applications like HSM [6,40].

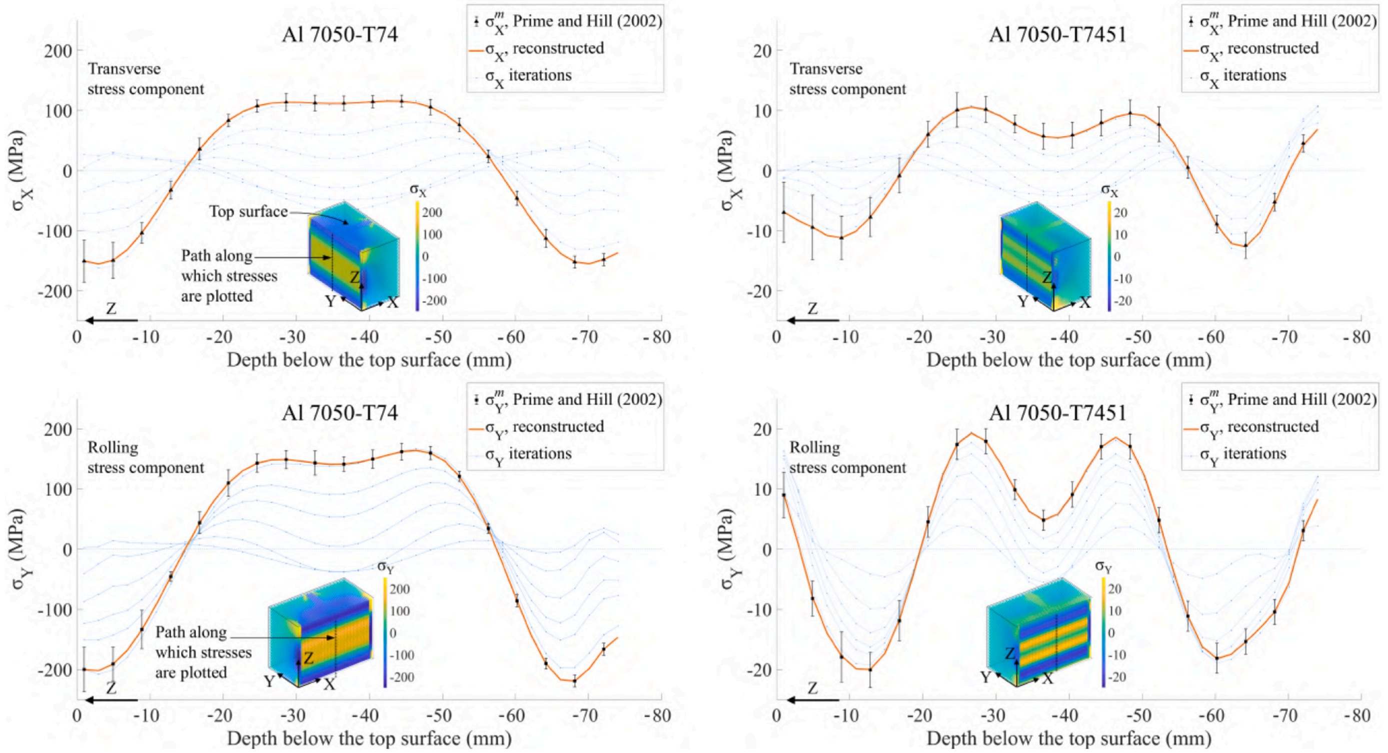

Fig. 3. Comparison of the reconstructed stress fields in the rolling (Y) and transverse (X) directions as a function of depth through the aluminum block, with those determined by Prime and Hill [3] via slitting method. The comparison is made along a path formed at the intersection of the central X and Y planes. The faint lines illustrate the variation of the rolling and transverse stress components, over the iterations, as they approach convergence. (*Inset*) 3D perspective of the reconstructed rolling and transverse stress components. (For interpretation of the reference to color in this figure, the reader is referred to the online version of this article.)

Table 2
Johnson-Cook plasticity model parameters for Al 7050 [44].

J-C Parameters	Value
A	463.4 MPa
B	319.5 MPa
n	0.32
C	0.027
$\dot{\varepsilon}_0$	1 s^{-1}
T_0	25°C
T_m	610°C
m	0.99

$$\sigma_f = \left[A + B\left(\boldsymbol{\varepsilon}^{pl}\right)^{n}\right]\left[1 + C\ln\left(\frac{\dot{\boldsymbol{\varepsilon}}^{pl}}{\dot{\boldsymbol{\varepsilon}}_0}\right)\right]\left[1 - \left(T^*\right)^{m}\right] \tag{5}$$

$$T^* = \begin{cases} 0 & T < T_0 \\ \left(\dfrac{T - T_0}{T_m - T_0}\right) & T_0 \leq T \leq T_m \\ 1 & T > T_m \end{cases} \tag{6}$$

In Eqs. (5) and (6), A is the yield stress of the bulk material at room temperature, B is the strain hardening modulus, C is the strain-rate hardening coefficient, $\boldsymbol{\varepsilon}^{pl}$ is the plastic strain, $\dot{\boldsymbol{\varepsilon}}^{pl}$ is the plastic strain rate, $\dot{\boldsymbol{\varepsilon}}_0$ is the reference strain rate, n is the work-hardening exponent, m is the thermal softening exponent, and T^* is the homologous temperature term, normalized between the ambient temperature, T_0, and the melting temperature of the material, T_m. The J-C constitutive model parameters for machining Al 7050, determined by Fu et al. [44] via split Hopkinson pressure bar (SHPB) experiments, are listed in Table 2.

During the milling process, both tensile tear/ductile type fracture and shear type fracture can occur in the vicinity of cut, as described by Liu et al. [45]. To replicate these phenomena in the machining simulation, both ductile and shear fracture mechanisms are implemented. Conventionally, ductile damage models would consider the dependence of equivalent plastic strain at damage initiation, γ_D, on stress triaxiality, η, and plastic strain rate, $\dot{\boldsymbol{\varepsilon}}^{pl}$, however, studies by Bai and Wierzbicki [46], Lou et al. [47], and Cao et al. [48] have revealed that fracture mechanics can also be influenced by the normalized third invariant of deviatoric stress, χ, which depends on the Lode angle, ϕ. Accordingly, Eqs. (7),(8),(9),(10),(11) present the phenomenological Lode angle dependent ductile damage model that predicts the onset of damage due to void nucleation, void growth and coalescence of porosities:

$$\omega_D = \int \frac{d\boldsymbol{\varepsilon}^{pl}}{\gamma_D\left(\eta, \chi(\phi), \dot{\boldsymbol{\varepsilon}}^{pl}\right)} = 1 \tag{7}$$

where, ω_D is the ductile criterion state variable that increases monotonically with plastic deformation. Changes in the ductile criterion state variable, $\Delta\omega_D$, calculated over successive time increments during the simulation are described by Eq. (8).

$$\Delta\omega_D = \frac{\Delta\boldsymbol{\varepsilon}^{pl}}{\gamma_D\left(\eta, \chi(\phi), \dot{\boldsymbol{\varepsilon}}^{pl}\right)} \geq 0 \tag{8}$$

The stress triaxiality, η, is expressed as the ratio of the hydrostatic stress, p, to the equivalent von Mises stress, q, as given by Eq. (9).

Table 3
Johnson-Cook damage model parameters used in the high-speed machining model [49].

d_1	d_2	d_3	d_4	d_5
0.1009	0.1214	-0.915	-0.16789	0.877675

$$\eta = \frac{-p}{q} \tag{9}$$

The normalized third invariant of deviatoric stress, χ, can be expressed as a function of the Lode angle, ϕ, as shown in Eq. (10).

$$\chi = \cos(3\phi) = \left(\frac{r}{q}\right)^3 \tag{10}$$

where, r is the third invariant (or determinant) of deviatoric stress tensor, $\boldsymbol{\sigma}_s$, defined by Eq. (11).

$$r = \left(\frac{9}{2}\boldsymbol{\sigma}_s \cdot \boldsymbol{\sigma}_s : \boldsymbol{\sigma}_s\right)^{\frac{1}{3}} \tag{11}$$

The ductile damage criterion presented in Eq. (7) captures the influence of plastic strain-rate, however, it does not have any temperature specific term to capture the effect of thermal softening in the material. Thus, an additional J-C ductile damage criterion, given by Eq. (12), is introduced in the model to capture damage that results from both strain-rate and thermal softening in the material.

$$\gamma_D = \left[d_1 + d_2 e^{d_3 \eta}\right]\left[1 + d_4 \ln\left(\frac{\dot{\boldsymbol{\varepsilon}}^{pl}}{\dot{\boldsymbol{\varepsilon}}_0}\right)\right]\left[1 + d_5 T^*\right] \tag{12}$$

In Eq. (12), d_1 is the initial fracture strain, d_2 to d_5 represent the exponential, triaxial, strain-rate, and temperature parameters, respectively. The J-C damage parameters used in this study are listed in Table 3. Note, in lieu of J-C damage parameters for Al 7050, damage parameters for Al 7068 have been implemented. This is justified considering that the purpose of this work is to study the influence of IRS on HSM, rather than conducting a rigorous prediction of the damage evolution itself.

The shear damage criterion implemented in this work, described by Eqs. (13),(14),(15), is a phenomenological model that predicts the onset of damage due to shear band localization. It assumes that the equivalent plastic strain at damage initiation, γ_S, is a function of shear stress ratio, τ_S, and plastic strain-rate, $\dot{\boldsymbol{\varepsilon}}^{pl}$. A monotonic increase in the shear criterion state variable, $\Delta\omega_S$, occurs with the onset of plastic deformation proportional to the incremental change in γ_S until Eq. (13) is satisfied.

$$\omega_S = \int \frac{d\boldsymbol{\varepsilon}^{pl}}{\gamma_S\left(\tau_S, \dot{\boldsymbol{\varepsilon}}^{pl}\right)} = 1 \tag{13}$$

With successive time increments during the simulation, Eq. (14) computes the change in the shear criterion state variable, $\Delta\omega_S$.

$$\Delta\omega_S = \frac{\Delta\boldsymbol{\varepsilon}^{pl}}{\gamma_S\left(\tau_S, \dot{\boldsymbol{\varepsilon}}^{pl}\right)} \geq 0 \tag{14}$$

The shear stress ratio is described by Eq. (15), where k_S is a material parameter with a typical value of 0.3 for aluminum [50] and τ_{max} is the shear yield strength defined as $0.577A$ as per distortion-energy theory.

$$\tau_S = \frac{(q + k_S p)}{\tau_{max}} \tag{15}$$

The ductile damage and shear damage loci are referenced from Cao et al. [51]. Once damage is initiated, the damage evolution model, given by Eq. (16), empirically describes the rate at which the material stiffness degrades.

$$\boldsymbol{\sigma} = (1 - D)\boldsymbol{\sigma}^* \tag{16}$$

In Eq. (16), $\boldsymbol{\sigma}$ is the stress tensor computed at any instant during the simulation, while $\boldsymbol{\sigma}^*$ represents the undamaged stress tensor. The overall damage variable, D, is defined by Eq. (17).

$$D = \max(d_i) \tag{17}$$

As per Eq. (17), D is determined by the greatest scalar normalized damage variable, d_i, from the set of active damage mechanisms in the

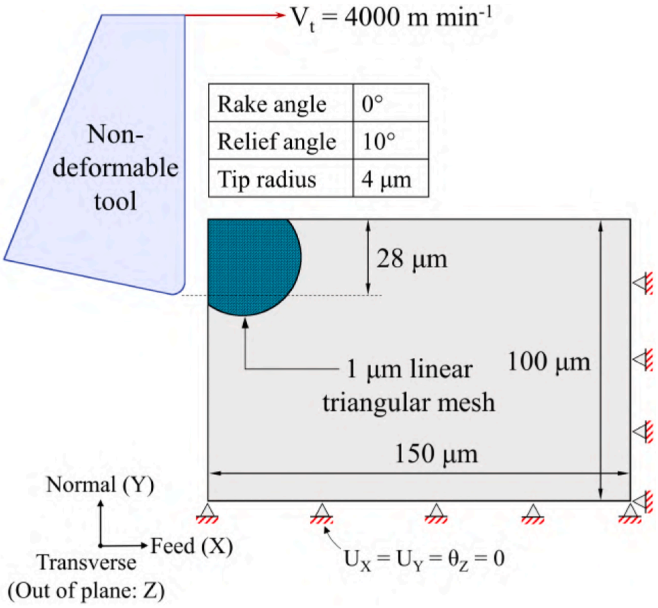

Fig. 4. Illustration of the 2D plain-strain orthogonal cutting model.

model at any given time increment. Considering reduced integration used in both the 2D and 3D models, every element has a single integration point located at its centroid. When the value of D becomes 1 at any integration point, the material loses its load-bearing capacity, and the element is deleted from the mesh.

After damage initiation, an energy-based exponential evolution law, described by Eq. (18), ensures that energy dissipation during damage evolution is equal to the fracture energy per unit area. It defines the relationship between the normalized damage variable, d, fracture energy per unit area, G_f, material yield strength, A, and effective plastic distortion at the point of failure, U^{pl}.

$$d = 1 - \exp\left(-\int_0^{U_f^{pl}} \frac{A}{G_f} dU^{pl}\right) \tag{18}$$

Since the 3D machined part is a high aspect-ratio structure, Rayleigh damping is implemented to dissipate any excess energy that can cause undesired and/or unrealistic vibrations in the material [52]. As described in Eq. (19), for the jth mode of vibration, the critical damping fraction, ξ_j, can be expressed in terms of mass proportional damping, α_R, stiffness proportional damping, β_R, and the corresponding natural frequency of the material, ω_j. Details regarding the damping constants implemented herein for aluminum are referenced from [53].

$$\xi_j = \frac{\alpha_R}{2\omega_j} + \frac{\beta_R \omega_j}{2} \tag{19}$$

3.2. Two-dimensional orthogonal cutting model

To validate the aforementioned material and damage definitions, a 2D orthogonal cutting model that assumes plain-strain is built. As illustrated in Fig. 4, a planar 150 μm × 100 μm section of the Al 7050 workpiece is discretized using a uniform, 1 μm, linear triangular element mesh. Translation and rotary motion of two orthogonal edges of the workpiece are constrained, as seen in Fig. 4. Since any possible effects of tool deformation and thermal conduction into the tool are deemed negligible, considering computational efficacy, a non-deformable tool is modeled and represented as an analytical rigid body. The tool has a rake angle of 0°, a relief angle of 10°, and a tip radius of 4 μm. The tool is assigned a feed velocity (V_t) of 4000 m min^{-1} as per [54] and is positioned to give a cut depth (Y direction) of 28 μm.

Table 4
Summary of the 2D orthogonal cutting case studies demonstrated in this work.

Case study	IRS present	IRS profile
2D-Ref.	No	N/A
2D-1	Yes	Profile 1
2D-2	Yes	Profile 2

Since the HSM simulation couples thermal and mechanical solutions, heat is generated due to the combined effects of plastic work and friction at the tool-workpiece interface. The heat flux per unit volume, q_p, associated to plastic strain heat dissipation, is expressed by Eq. (20), where Ψ (98%) is the plastic heat dissipation fraction [55].

$$q_p = \Psi \boldsymbol{\sigma} : \dot{\boldsymbol{\varepsilon}}^{pl} \tag{20}$$

Heat flux generated via Coulomb friction, q_f, described in Eq. (21), is the product of the friction heat generation fraction, ψ (95%) [56], incremental slip rate, $\dot{s}$, and frictional stress, σ_{fric}, that is a function of the contact pressure, coefficient of friction (0.33) [57,58], and tool-workpiece interface temperature.

$$q_f = \psi \dot{s} \sigma_{fric} \tag{21}$$

Heat loss is modeled via conduction and convection, while the effect of heat radiation, being comparatively negligible, has been omitted.

In addition to validating the material and damage definitions, a set of case studies for the 2D orthogonal cutting model, summarized in Table 4, are investigated to elucidate the effect of IRS on the resulting stress in HSM.

Two IRS profiles are modeled in Cases 2D-1 and 2D-2, respectively, based on work by Zhang et al. [59] wherein a methodology to model RS in stretch-stress relieved wrought aluminum blocks was described. The IRS profiles implemented in the two cases, although similar in range of magnitude (-30 to 30 MPa), vary in spatial distribution. Results from the 2D case studies are presented and discussed later in Section 4.1.

While the 2D model is utilized to investigate the effect of IRS on RS profiles that emerge from HSM, a 3D model, discussed next, is employed to investigate the effect IRS has on the distortions that arise by end-milling high aspect-ratio structures from the wrought aluminum block.

3.3. Three-dimensional end-milling model

A 3D end-milling model is used to examine the effect IRS has on the distortion that arises in high aspect-ratio monolithic structures. For this study, as illustrated in Fig. 5, a C-channel is machined from two wrought Al 7050 blocks that have different IRS profiles. As mentioned earlier, the dimensions of the aluminum blocks are 100 mm × 100 mm × 75 mm, and they are discretized using linear hexahedral elements having an approximate edge length of 2 mm. Translational motion on the bottom face of the workpiece is constrained, as seen in Fig. 5, while no other boundaries are constrained. This is done to omit additional stresses that may be induced in the workpiece during clamping. A non-deformable square-end mill tool has been modeled as a discrete rigid body, featuring 3 mm linear triangular shell elements, to reduce computational time. The tool features 3 flutes (z = 3), a 30° helix angle, and a 30 mm diameter.

For each pass of the tool, an axial cut depth (Z direction) of 34.5 mm is considered. The machining parameters include a feed per tooth, F_n, of 0.343 mm/tooth (1.14% of the tool diameter) and a spindle speed, N, of 35,000 RPM. Accordingly, the linear feed velocity, V_f, and angular velocity, ω_t, of the tool is given by Eqs. (22) and (23).

$$V_f = \frac{F_n z N}{60} \approx 0.6\ \mathrm{m\ s^{-1}} \tag{22}$$

$$\omega_t = \frac{2\pi N}{60} \approx 3665\ \mathrm{rad\ s^{-1}} \tag{23}$$

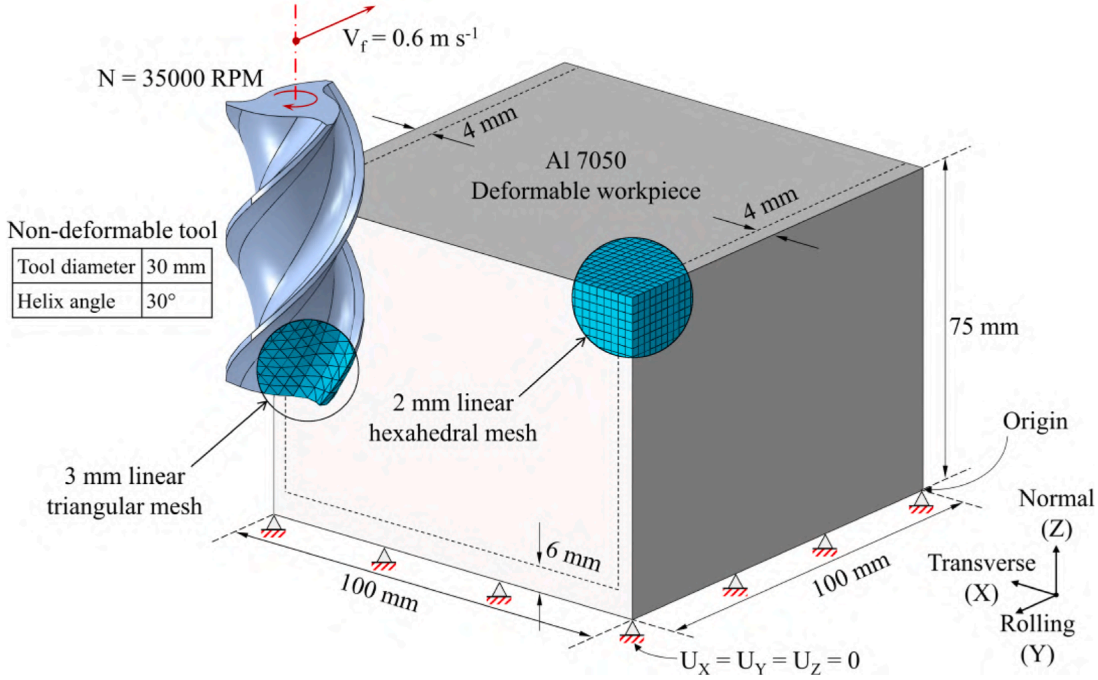

Fig. 5. Illustration of the 3D end-milling model.

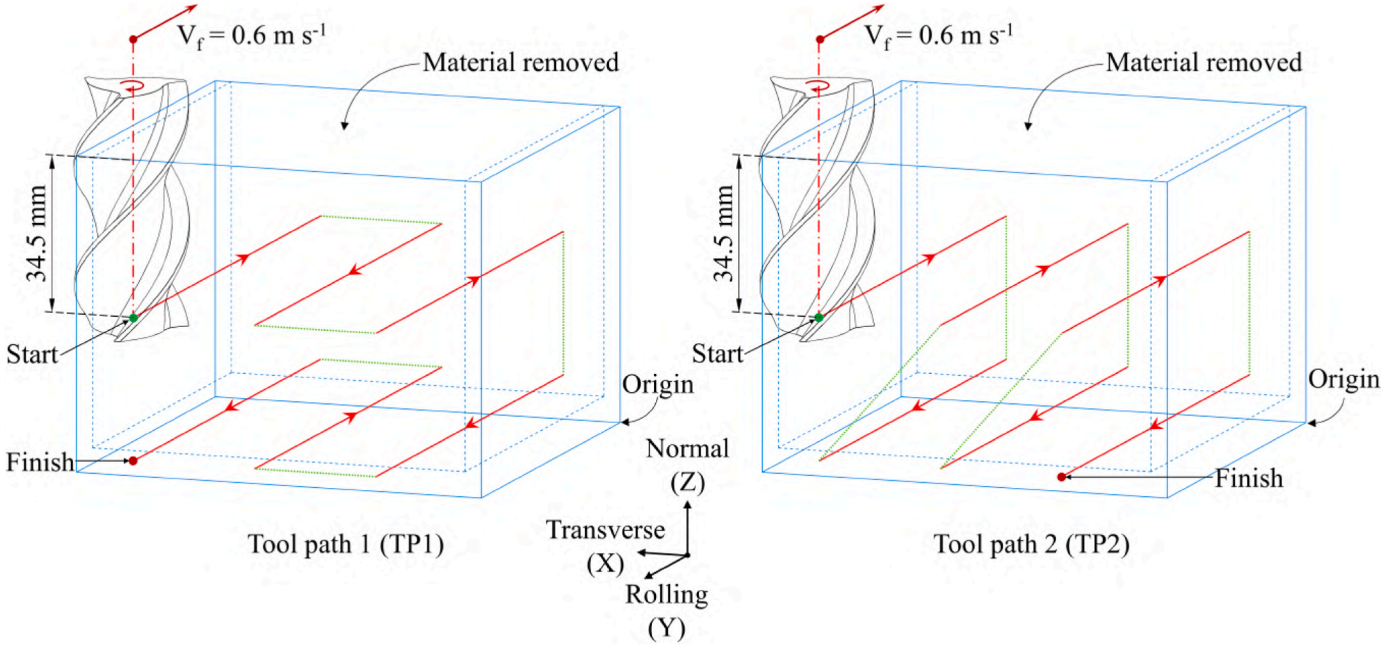

Fig. 6. End-milling tool paths considered in the 3D HSM model (ref. Table 5). Net volume of material removed, represented by the dotted line, is the same for both tool paths.

Table 5
Summary of the 3D end-milling case studies demonstrated in this work.

Case study	Tool path	IRS pattern (ref. Fig. 3)	IRS magnitude range
3D-1	Tool path 1 (TP1)	No IRS	N/A
3D-2	TP1	T74	High, -200 to 200 MPa
3D-3	TP1	T7451	Low, -20 to 20 MPa
3D-4	Tool path 2 (TP2)	No IRS	N/A
3D-5	TP2	T74	High, -200 to 200 MPa
3D-6	TP2	T7451	Low, -20 to 20 MPa

Note that the machining process parameters in this study may not exactly represent those in the corresponding practical machining operation due to machining power and/or stability limitations. Specifically, a relatively large axial depth of cut is employed in the 3D model to facilitate computational feasibility. Nonetheless, modeling of such machining parameters still satisfies the purpose of the investigation, which is to elucidate the effects of IRS within the wrought Al 7050 block on the distortion that arises when end-milling high aspect-ratio monolithic structures, like the C-channel for example. Accordingly, a set of case studies, summarized in Table 5, are investigated. For each tool path, shown in Fig. 6, three cases are simulated based on differing IRS profiles:

(1) Cases 3D-1 and 3D-4 are modeled without IRS and are considered to be reference cases. (2) Cases 3D-2 and 3D-5 are modeled with relatively high IRS magnitudes (-200 to 200 MPa) and a spatial distribution as per Prime and Hills measurements [3] on the T74 specimen (ref. Fig. 3). (3) Cases 3D-3 and 3D-6 are modeled with relatively low IRS magnitudes (-20 to 20 MPa) and a spatial distribution as per Prime and Hills measurements on the T7451 specimen which was stretch stress relieved (ref. Fig. 3). The corresponding converged (and compatible) IRS from ISRA are implemented as initial conditions in the 3D end milling simulation, per Eq. (24).

$$\boldsymbol{\sigma}(\mathbf{X},0) = \boldsymbol{\sigma}^k_{\mathrm{ij}}(\mathbf{X}) \tag{24}$$

Dynamic thermomechanical solutions to the 2D orthogonal cutting simulations, as well as the 3D end-milling simulations, are computed using the explicit solver of Abaqus v6.14. Results for both the 2D and 3D cases are presented and discussed next.

4. Results and discussion

The effects of IRS on residual stress profiles that emerge from HSM are discussed in Section 4.1, following a comparison of the predicted temperature, shear banding, and chip morphology with experimental observations documented in the literature to validate the material and damage models implemented. The influence IRS has on distortion that arises when machining high aspect-ratio components is discussed in Section 4.2.

4.1. Two-dimensional orthogonal cutting

The demonstrated modeling approach applied in the 3D HSM cases (ref. Table 5) is first validated by comparing 2D micro-scale orthogonal cutting simulations with findings and observations reported in the literature. For Case 2D-Ref. in Table 4, featuring no IRS in the bulk material, the resulting instantaneous spatial distribution of temperature, depicted in Fig. 7 (*Left*), is seen to closely resemble predictions documented in earlier work by Jomaa et al. [60], Wang and Liu [54], and Mabrouki et al. [61]. In HSM of aluminum alloys, much of the heat generated due to frictional and plastic work along the cut surface is lost via heat conduction through the chips, limiting the maximum predicted temperature at the cut surface to 150°C. The elevated temperatures are confined to within tens of micrometers beneath the cut surface. Adiabatic shear banding, illustrated in Fig. 7 (*Top right*) is revealed by re-mapping the spatially distributed equivalent plastic strain, γ_{eq}, onto the undeformed specimen. Similar findings have been experimentally observed by Dao et al. [62] as well as numerically predicted by Owen et al. [63] and Thomas et al. [64]. The predicted shear plane angle ($\varphi_\tau = 44°$) is similar to the range ($35° < \varphi_\tau < 42°$) analytically determined by Fang et al. [65] for the same cutting speed. These shear bands within the material removed, are also identified through the von Mises stress, σ_{vM}, distribution illustrated in Fig. 7 (*Bottom right*). As mentioned earlier, once an element is damaged ($D = 1$), the load-bearing capacity is lost, as reflected by zero σ_{vM} in the figure.

The distribution of machining-induced residual stress (MIRS) along the feed (X), normal (Y), and transverse (Z) directions is depicted in Fig. 8. A quantitative analysis of the averaged MIRS as a function of depth from the cut surface is performed within the "region of interest" encompassed by the dashed rectangle. Referring to Fig. 9, the MIRS averaged along the feed direction, at different depths beneath the cut surface, shows good agreement with neutron diffraction measurements documented by Li and Wang [66] whose work featured similar cutting parameters. At distances ranging from 10 to 60 μm, the MIRS predicted from the demonstrated model falls within experimental error limits, in the feed (X) and transverse (Z) directions. Variations between the predicted and experimental MIRS as a function of depth from the cut surface arise considering that the specimen used by Li and Wang had an inherent residual stress (IRS) field, whereas the predicted MIRS from Case 2D-Ref. in Table 4, is modeled without any IRS. The simulated chips shown in the inset image in Fig. 9 geometrically resemble those experimentally observed by Wang and Liu [54] whose work featured the same cutting parameters. Hence, the material model implemented herein can predict chip formation and chip morphology with reasonable accuracy.

Fig. 10 (*Top and Bottom*), respectively, show (*Left to Right*) feed (X), normal (Y) and transverse (Z) components for two different IRS profiles (blue dash-dot line) modeled in the specimen. The differing IRS profiles are implemented in Cases 2D-1 and 2D-2, introduced earlier in Table 4. The figures also show the predicted final-state residual stress, FRS (red line), in the bulk material at the end of the machining process, and the machining-induced residual stress, MIRS (black line), obtained by neglecting the IRS during the machining simulation. For both cases, the cutting process parameters remain the same as those depicted earlier in Fig. 4. Note, the FRS and MIRS are averaged along the feed (X) direction, within the region of interest (ref. Fig. 8) and expressed as a function of distance from the cut surface. In addition, for both cases, the normalized root mean square deviation (NRMSD) for the FRS and the IRS has been

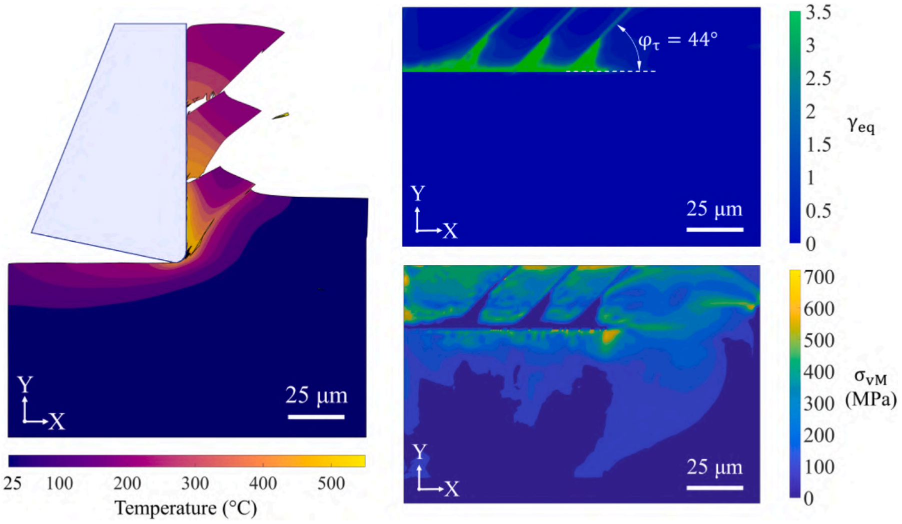

Fig. 7. (*Left*) Instantaneous spatial distribution of temperature for Case 2D-Ref. Adiabatic shear banding revealed via: (*Top right*) equivalent plastic strain (re-mapped onto undeformed model), and (*Bottom right*) von Mises stress (re-mapped onto undeformed model). (For interpretation of the reference to color in this figure, the reader is referred to the online version of this article.)

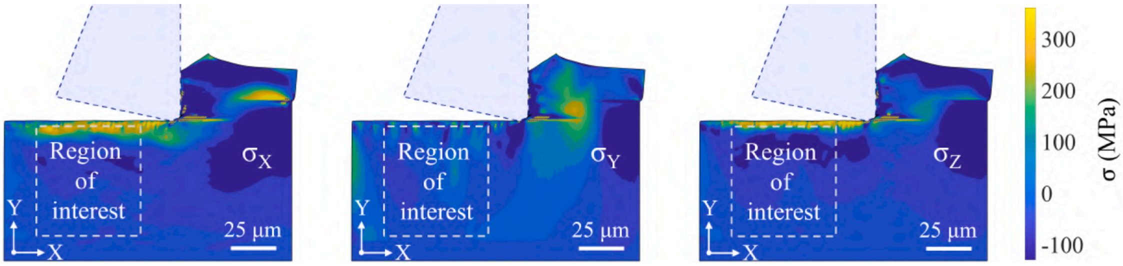

Fig. 8. (*Left to Right*) Machining-induced residual stress (MIRS) along the feed (X), normal (Y), and transverse (Z) directions, respectively. The dashed rectangle represents the region of interest for which a quantitative comparison with Li and Wangs experimental observations [66] is presented in Fig. 9. Note, the tool shown in figure is only representative of the final position of the tool before it was moved away from the workpiece. (For interpretation of the reference to color in this figure, the reader is referred to the online version of this article.)

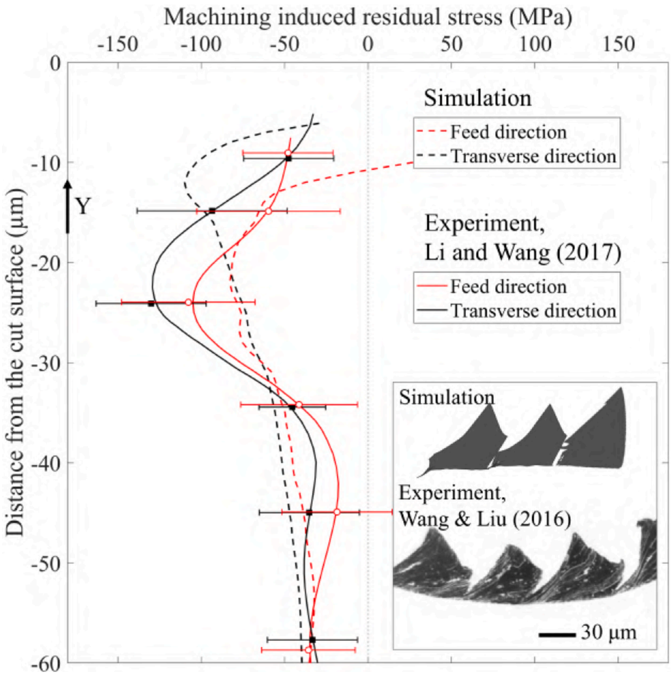

Fig. 9. Comparison of the predicted machining-induced residual stress, in the feed (X) and transverse (Z) directions, with neutron diffraction measurements by [66]. (*Inset*) Comparison of chip morphology simulated in this work with those experimentally imaged by [54] whose work featured the same cutting parameters. (For interpretation of the reference to color in this figure, the reader is referred to the online version of this article.)

computed for the individual components. The $\mathrm{NRMSD}_{\mathrm{FRS}}$ computes the root mean square difference (RMSD) between the FRS and MIRS through the depth of the material and normalizes it over the range of the MIRS. The $\mathrm{NRMSD}_{\mathrm{IRS}}$ computes the RMSD between the IRS and a null stress state through the depth of the material (post-machining) and normalizes it over the range of the MIRS.

The trends observed in Fig. 10 are as follows:

- The distribution and magnitude of FRS for individual component, i.e., feed (X), normal (Y), and transverse (Z), do not coincide. While the trends seen herein, between Cases 2D-1 and 2D-2 for the feed and transverse components appear somewhat similar, the same is not true for the normal (Y) component. Comparing the $\mathrm{NRMSD}_{\mathrm{FRS}}$ for the individual components, between Cases 2D-1 and 2D-2, it is quantitatively evident that the feed (X) and transverse (Z) components are susceptible to the influence of IRS, with values less than 8%. Comparatively, the normal (Y) component appears to show significant $\mathrm{NRMSD}_{\mathrm{FRS}}$, i.e., 23.76% (Case 2D-1) and 51.41% (Case 2D-2). This reveals that IRS indeed influences the state of stress in the bulk material post-machining and hence should not be overlooked when building numerical models for HSM. Furthermore, the degree of influence of IRS components on corresponding components of FRS is found to vary significantly, indicating that a priori knowledge of IRS magnitude and distribution can be useful in determining the choice of tool path.
- The $\mathrm{NRMSD}_{\mathrm{FRS}}$ for individual stress components is greater than the corresponding $\mathrm{NRMSD}_{\mathrm{IRS}}$. Interestingly, the $\mathrm{NRMSD}_{\mathrm{FRS}}$ is found to be appoximately 3.5 times greater than the corresponding $\mathrm{NRMSD}_{\mathrm{IRS}}$, for the normal (Y) component in both cases. Given that similar scaling factors cannot be determined for the remaining two components suggests that the inclusion of IRS in the model can have an anisotropic effect on the magnitude of FRS post-machining.
- The FRS in the feed (X) direction (σ_X), at depths of 1 to 9 μm from the cut surface, appears to have more tension (Case 2D-1) as well as less tension (Case 2D-2) than the corresponding MIRS. The only differing feature in the IRS is the tensile/compressive trend at depths of 20 to 40 μm. Additionally, The FRS in the feed direction (σ_X), at depths of 10 to 30 μm from the cut surface, appears to have less compression than the MIRS. The only common feature in the IRS distribution is the tensile state within the material removed. Furthermore, the FRS in the normal (Y) direction (σ_Y), at depths of up to 2 μm from the cut surface, is predicted to vary considerably between the two cases. The only difference in the IRS distribution observed for the same component, near the cut surface, is within the section of material removed. Hence, the state of IRS in the material removed is found to have some influence on the resulting FRS distribution and magnitude in the bulk material.
- Contrary to the trends observed between the MIRS and FRS for the feed (X) and normal (Y) components, the trends observed for the transverse (Z) components reveal that the FRS is an approximate superposition of the IRS and MIRS, i.e., IRS + MIRS ≈ FRS. It should be noted, however, that the 2D orthogonal cutting model assumes plain-strain conditions in the transverse direction, and hence the principle of superposition may not necessarily be applicable in a 3D model.

The foregoing discussion supports the first hypothesis of this work such that the FRS in the machined aluminum components is indeed influenced by IRS, and the degree of influence of IRS on the corresponding FRS does indeed vary based on the IRS profile (i.e., magnitude and distribution).

While the 2D orthogonal cutting simulation offers important insights on how the FRS is influenced by the IRS while revealing good agreement with experimental observations documented in the literature, a full-scale 3D HSM model would necessitate reducing the mesh density to ensure computational feasibility. This limits the accuracy of predicting details such as temperature distribution and RS that are best captured using more a refined mesh. Nevertheless, validity of the numerical

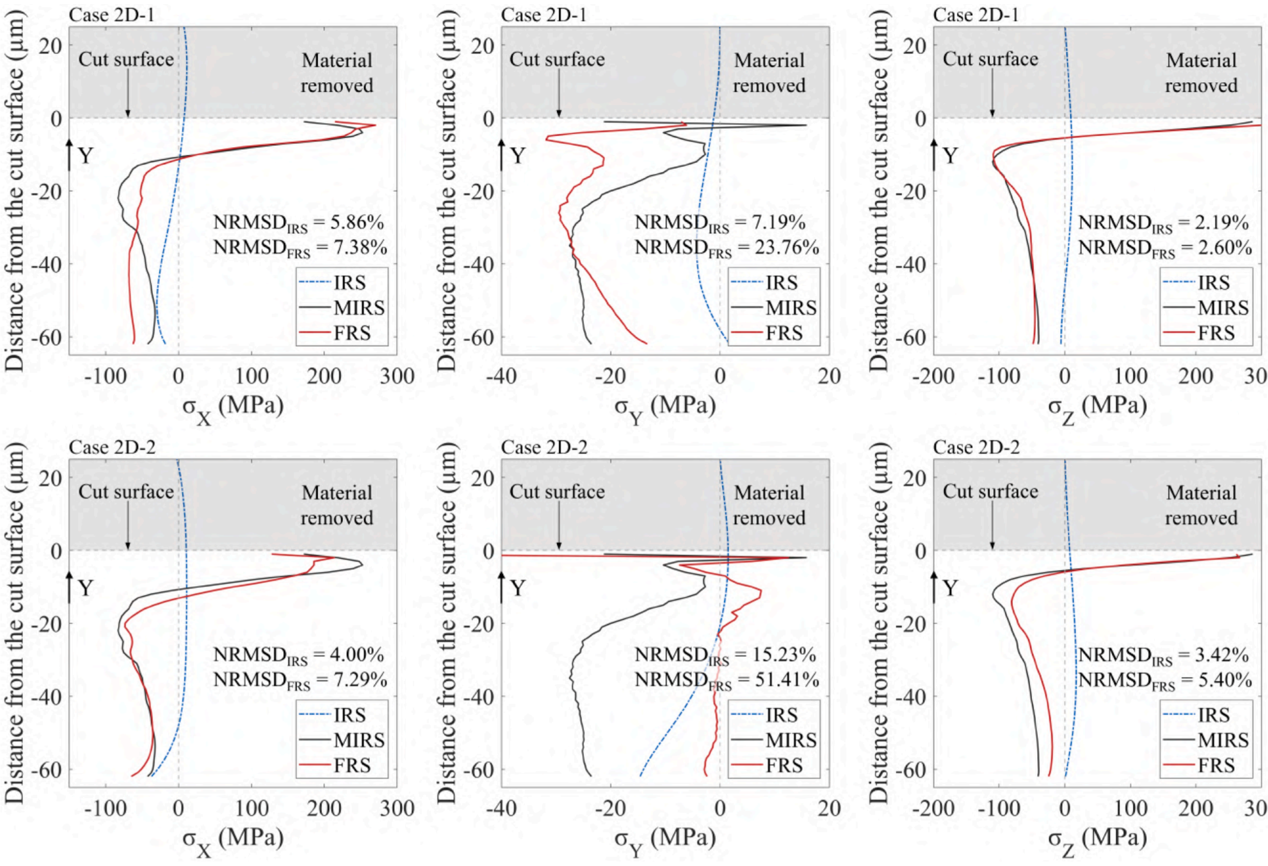

Fig. 10. Inherent residual stress (IRS), machining-induced residual stress (MIRS), and the final-state residual stress (FRS), as a function of distance from the cut surface, in (*Left to Right*) the feed (X), normal (Y) and transverse (Z) directions, respectively, for Cases 2D-1 (*Top*) and 2D-2 (*Bottom*). Note, the range of stress for the normal component is significantly lower than that of the feed and transverse components. NRMSD$_{MIRS}$ represents the root mean square deviation between FRS and MIRS, normalized by the range of MIRS. NRMSD$_{IRS}$ represents the root mean square deviation between IRS and null stress state, normalized by the range of MIRS. (For interpretation of the reference to color in this figure, the reader is referred to the online version of this article.)

approach is still retained given that the demonstrated material and damage model remains unchanged for the 3D end-milling model, wherein distortion is investigated when machining a C-channel from a wrought aluminum block, as discussed next.

4.2. *Distortion arising from 3D end-milling of a C-channel*

The distortion in the X direction (ΔX) that results from the end-milling simulation, for each of the 6 case studies described earlier in Table 5, is depicted in Fig. 11. The top row features milling induced distortion when implementing tool path 1 (TP1) for different cases of IRS, i.e., no IRS, high IRS (T74 specimen), and low IRS (T7451 specimen). The bottom row features the same when implementing tool path 2 (TP2). The net volume and location of material removed is the same with both tool paths and the undeformed (desired) C-channel geometry is represented by the dotted lines. For brevity, only the distortion in the X direction (ΔX) is discussed herein considering that distortions predicted in the Y and Z directions are less prominent. The averaged wall thickness ratio (WTR), defined herein as the ratio of the averaged wall thickness at the top of the flange to that at the bottom, reveals that change in the IRS profile does not result in significant WTR variation ($<$ 0.5%). Whereas, with respect to tool path, for the left-sidewall a WTR variation of about negative 4% is predicted from TP1 to TP2, while for the right-sidewall a WTR variation of about positive 19% from TP1 to TP2 is predicted. This indicates that, for the cases examined, tool path strategy plays a larger role in wall thickness uniformity compared to the IRS. Since the thin walls being machined have an aspect-ratio (height : thickness) of 17.25:1, the top (or free) edges are susceptible to considerable amounts of distortion. For Cases 3D-1 and 3D-4 in Table 5, featuring no IRS, the distortions averaged along the Y direction, $\overline{\Delta X}$, at the top outer edges of the machined specimen are also determined, as seen in Fig. 11. The $\overline{\Delta X}$ calculated for the other cases at the same locations are relatively similar in magnitude.

Comparing ΔX for all 6 cases the following observations are made:

- The qualitative trends in ΔX, as well as quantitative trends when comparing $\overline{\Delta X}$ clearly differ based on the choice of tool path; For TP1, a relatively symmetric ΔX distribution about the plane X = 50 mm is revealed, however, the same is not true for TP2. Quantitatively, for TP2, the absolute distortion at the top edge of the right-sidewall is approximately 2.5 times greater than that on the left-sidewall.
- The amount of deflection (or distortion) predicted during a milling pass depends on the net volume and location of the bulk material that has already been removed. In addition, during the machining operation, if certain segments of geometry are created that have high aspect-ratios, there will likely be more distortion in such segments, as the machining operation progresses; Half-way into the machining operation for TP1, considering the 34.5 mm axial depth of cut (Z direction), the left- and right-sidewall segments have an aspect-ratio of 8.625:1, whereas, Half-way into the machining operation for TP2, the right-sidewall segment has an aspect-ratio of 17.25:1, while the left-sidewall has an aspect-ratio of 8.625:1. Hence, TP1 results in a more symmetric ΔX distribution compared to TP2.

For each tool path, comparing the different cases of IRS, i.e., no IRS,

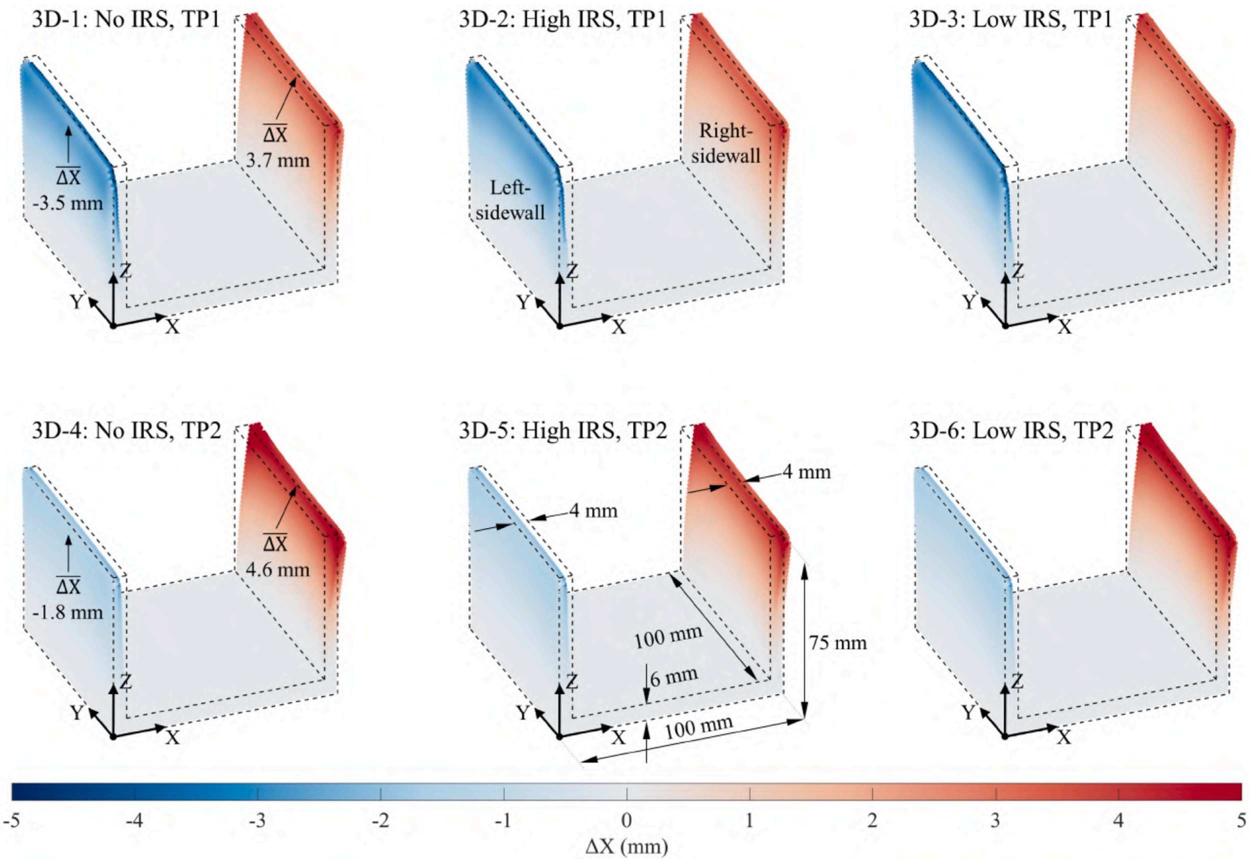

Fig. 11. Distortion in the X direction (ΔX) for the 6 case studies described earlier in Table 5. The dotted lines represent the undeformed (or desired) final geometry. ($\overline{\Delta X}$) denotes the distortions averaged along the Y direction at the top outer edges of the flanges of the machined specimen. (For interpretation of the reference to color in this figure, the reader is referred to the online version of this article.)

high IRS (T74 specimen), and low IRS (T7451 specimen), no apparent difference in ΔX is revealed. Thus, the effect of IRS on distortion is not directly discernible from Fig. 11 and the relative difference in distortion, as depicted in Fig. 12, needs to be assessed to elucidate the relationship between IRS and the distortion that results from HSM.

According to [11,14], the final-state distortion can be predicted via a linear superposition function of the IRS-induced distortion and MIRS-induced distortion. Hence, if the distortion from Case 3D-1 is subtracted from that of Cases 3D-2 and 3D-3, the *relative* distortion resulting from each of the two IRS profiles would be obtained for TP1, as seen in Fig. 12 (*Top left*) and (*Top right*), respectively. Similarly, if the distortion from Case 3D-4 is subtracted from that of Cases 3D-5 and 3D-6, the relative distortion resulting from each of the two IRS profiles would be obtained for TP2, as seen in Fig. 12 (*Bottom left*) and (*Bottom right*), respectively. Having removed the effect of machining, and isolating the influence of IRS, the relative distortions pictured in Fig. 12 (*Top left*) and (*Bottom left*), featuring IRS determined from the T74 specimen, or Fig. 12 (*Top right*) and (*Bottom right*), featuring IRS determined from the T7451 specimen, should coincide, however, that is not observed.

Two plausible explanations for this are: (1) IRS induced distortion is influenced by the choice of tool path [12], and (2) for a given tool path, machining-induced distortion varies with different IRS profiles.

In regard to the IRS-induced distortion, since IRS is always in the elastic regime, distortions caused by material removal would inevitably resolve to elastic stress distributions. Thus, for the same net volume and location of material removed, any tool path will result in the same IRS-induced distortion, neglecting all clamping and machining-induced effects. Whilst this cannot be tested experimentally, it can be studied via numerical approaches like element deletion [15,17]. This contradicts the findings of [12], who determined that IRS-induced distortion is influenced by the choice of tool path.

Since the relative distortions for a given IRS profile, as seen in Fig. 12, do not coincide, the machining-induced distortion captured in each of the different case studies, depicted in Fig. 11, is found to differ. Contrary to assumptions made by [11,14] the final distortion is a non-linear function of IRS and MIRS, rather than a linear superposition of the two. The demonstrated work and findings presented illuminates the fact that a coupling does indeed exists between IRS and MIRS. Hence, the second hypothesis in this work is supported.

The relative distortion in the X direction (or relative ΔX) for the four cases depicted in Fig. 12, are plotted as a function of the height (Z direction), in different regions of the C-channel, as illustrated in Fig. 13. Note, for each of the lines plotted, the effects of machining-induced distortion (independent of IRS) have been excluded, isolating the influence of IRS on the (relative) distortion. A secondary horizontal axis normalizes the relative ΔX as a fraction of the wall height (75 mm), to help identify the ratio of relative ΔX at the free end (or top edges) of the thin wall.

Comparing the relative ΔX in the six regions, the following observations can be made:

- Despite symmetry in the transverse IRS distribution (ref. Fig. 13 *Inset bottom right*) about the plane Y = 50 mm, the relative ΔX predicted along the red strips at the edges, i.e., max- and min-Y, on both the left- and right-sidewalls, reveals asymmetric distortion patterns about the same plane of symmetry. Similarly, despite symmetry in the rolling IRS distribution about the plane X = 50 mm, the relative ΔX predicted along the red strips on both the left- and right-sidewalls, reveals asymmetric distortion patterns about the same

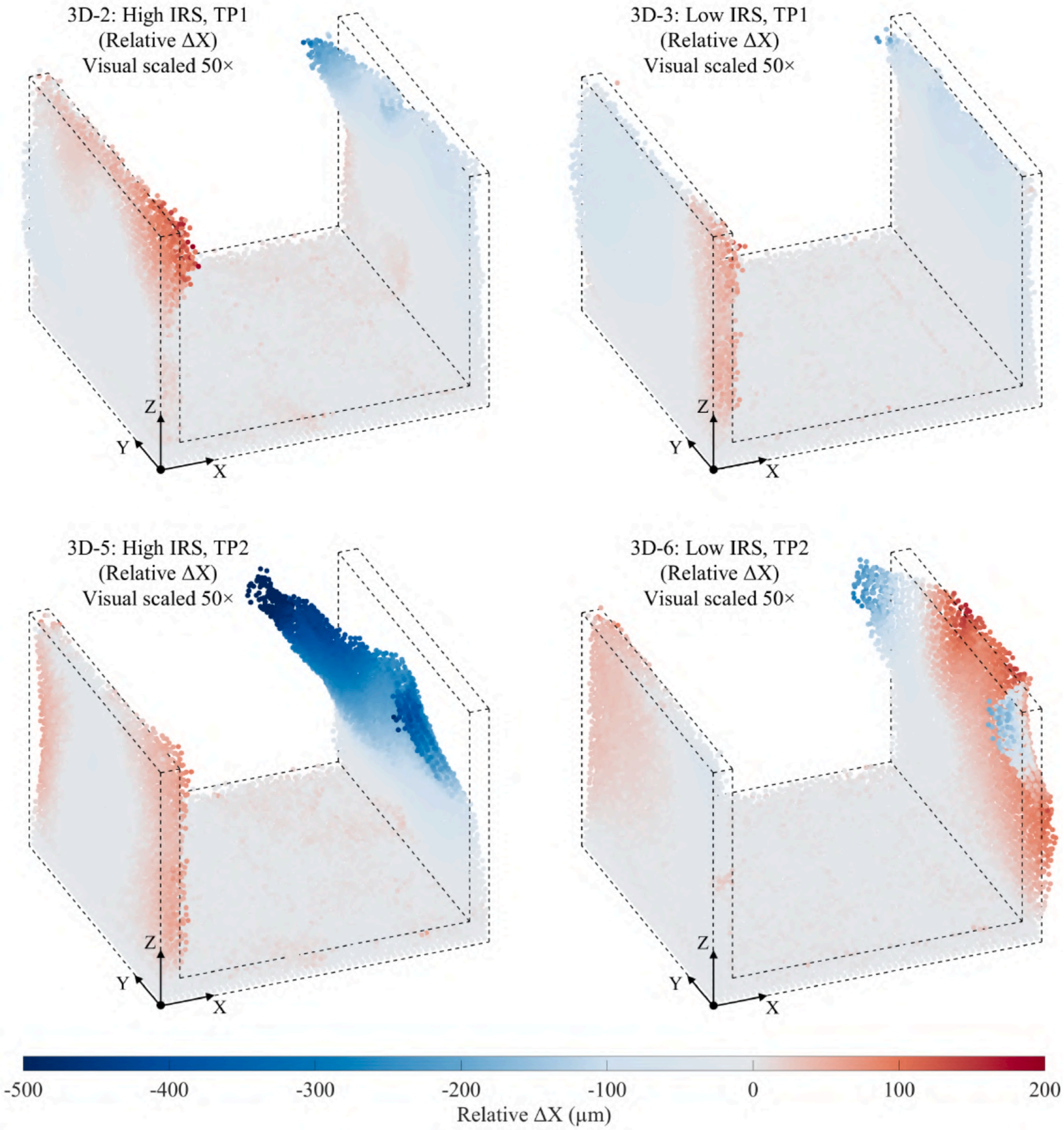

Fig. 12. (*Top*) Relative distortion in the X direction for Cases 3D-2 and 3D-3, obtained by subtracting the distortion for Case 3D-1 from each of them. (*Bottom*) Relative distortion in the X direction for Cases 3D-5 and 3D-6, obtained by subtracting the distortion for Case 3D-4 from each of them. A visual scale of 50× is used to emphasize the relative distortions. The dotted lines represent the undeformed (or desired) final geometry. (For interpretation of the reference to color in this figure, the reader is referred to the online version of this article.)

plane of symmetry. This is true for each of the four cases depicted in Fig. 13, illuminating the fact IRS cannot be solely responsible for the final distortion and that there must indeed exist a coupled effect between IRS and MIRS. Hence, the second hypothesis in this work is supported.

- The magnitude of relative ΔX predicted by the end-milling process is affected by the net volume and location of the bulk material that has already been removed. Considerable differences in the ΔX predicted for right- and left-sidewalls are evident from the predictions obtained when using tool path 2. Comparing the normalized distortions on the right-sidewall (ref. Fig. 13 *Top*) with that of the left-sidewall (ref. Fig. 13 *Bottom*) the dashed lines representing tool path 2 reveal relatively greater distortions on the right-sidewall, regardless of the underlying IRS profile implemented. These findings reveal that while the choice of tool path strongly influences the IRS-induced distortion, the underlying IRS profile also affects the degree by which the tool paths influence the IRS-induced distortion.
- The difference in relative ΔX when comparing Cases 3D-5 with 3D-6 and 3D-5 with 3D-2 (ref. Fig. 13) illuminates the influence of tool path on the coupling of MIRS and IRS. The reduction in relative ΔX from Case 3D-5 (High IRS, TP2) to Case 3D-2 (High IRS, TP1) is greater than the reduction in relative ΔX from Case 3D-5 (High IRS, TP2) to Case 3D-6 (Low IRS, TP2) in nearly all regions on the part. This result shows that distortion reduction achievable through choice of tool path is more significant than that achievable via IRS reduction (an order of magnitude reduction in this study). Hence, the third hypothesis in this work is supported.

While the 2D model (featuring a 1 μm mesh) presented in Section does capture variations in MIRS to within 10 to 100 μm from the cut surface, the 3D model includes but aggregates these highly localized

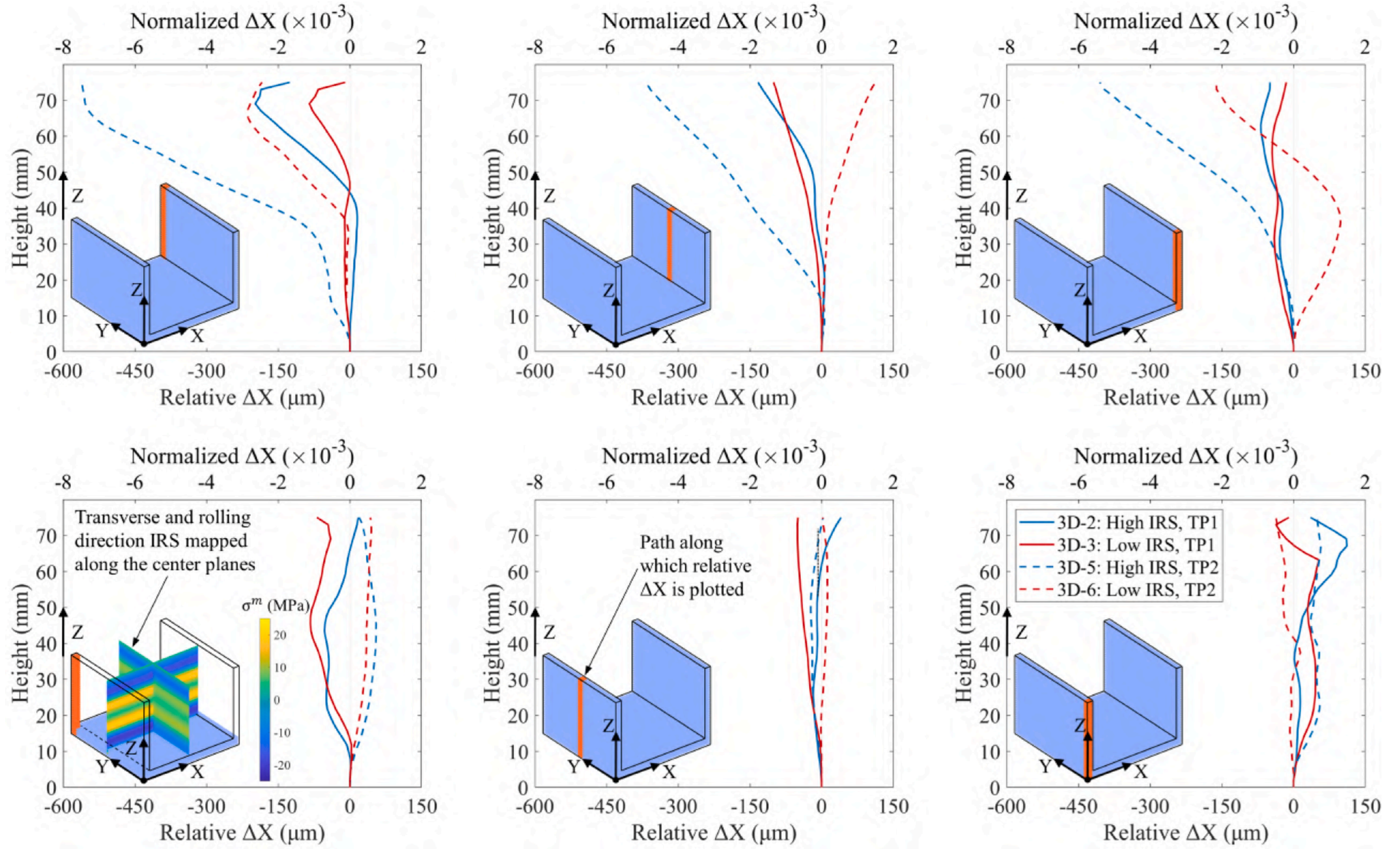

Fig. 13. Relative distortion considering the high inherent residual stress (IRS) patterns (from T74 specimen) and low IRS pattern (from T7451 specimen) machined using both tool paths, plotted as a function of wall height, in different regions of the (*Inset*) C-channel, represented by the orange regions. The normalized axis (*upper X-axis*) represents the relative distortions normalized by the wall height (75 mm). (*Inset bottom left*) An example of the measured IRS profile in the rolling (Y) and transverse (X) directions as per [3] that has been reconstructed in the wrought aluminum block. (For interpretation of the reference to color in this figure, the reader is referred to the online version of this article.)

effects of the tool-workpiece interaction (both mechanical and thermal) over the volume of the element. While the 3D model can be executed with a mesh much finer than 2 mm, considering computational feasibility, the 2 mm mesh is still found to be sufficient to reveal important and novel findings on the coupled effects discussed in this section. With the 2 mm mesh, the HSM simulations require ∼2 weeks run time (24 core Xeon E5-2670 v3, 2.3GHz, with 132 GB RAM), and this time will increase exponentially as the mesh is refined. Although the results obtained are specific to the IRS profiles, machining parameters, and final part geometry implemented in this work, and cannot be directly extrapolated to other conditions, the results demonstrate that there is indeed a nonlinear coupling interaction between IRS and MIRS.

5. Conclusions

This work investigates the coupled effects of inherent residual stress (IRS) and machining-induced residual stress (MIRS) on the final-state of residual stress (FRS) and distortion when high-speed machining (HSM) thin-walled monolithic aluminum components. Wrought Al 7050 blocks with two differing IRS profiles (based on stress relief) have been considered herein. To numerically model a spatially-complete and fully-compatible IRS field in the wrought aluminum blocks based on limited data from slitting measurements documented in the literature, an iterative stress reconstruction algorithm is implemented. A 2D orthogonal cutting model has been used to validate the material constitutive and damage models employed, and to elucidate the influences of IRS and MIRS on FRS. A 3D end milling model, which adopts the validated material and damage definitions, is applied with different tool paths to investigate the coupled effects of IRS and MIRS on the distortion when HSM a C-channel featuring high aspect-ratio walls. Several key findings are revealed from the study.

First, IRS influences the post-machining state of stress in the bulk material and hence should not be overlooked when building numerical models for HSM. Furthermore, the degree of influence of IRS components on the corresponding components of FRS is found to vary significantly. In addition, IRS in the bulk material has an anisotropic effect on the FRS and the state of IRS in the material removed is also found to influence the FRS profile. Therefore, a priori knowledge of the IRS profile can be useful in determining tool path strategy.

It is also found that the deflection (or distortion) predicted during a milling pass depends on the net volume and location of the bulk material that has already been removed; high aspect-ratio segments created earlier in the machining process are predicted to suffer greater distortion than those created later. Additionally, the final distortion is a nonlinear function of IRS and MIRS rather than a linear superposition of the two, indicating that a nonlinear coupling does indeed exist between IRS and MIRS. Moreover, due to this nonlinear coupling, the degree by which the tool path influences the IRS-induced distortion is affected by the underlying IRS profile. As a result, in this study, distortion reduction achievable through choice of tool path is more significant than that achievable via IRS reduction (by an order of magnitude). The nonlinear coupling between IRS and MIRS elucidated in this work reaffirms the need to mathematically optimize machining tool paths to achieve desired outcomes regarding final part geometry and state of stress.

Declaration of Competing Interest

The authors declare that they have no known competing financial interest or personal relationships that could have appeared to influence the work reported in this paper.

Acknowledgment

The authors acknowledge the support from U.S. National Science Foundation, grant no. CMMI-1762722. Any opinions, findings, or conclusions expressed in this paper are those of the authors and do not necessarily reflect the views of the U.S. National Science Foundation.

References

[1] Songmene V, Khettabi R, Zaghbani I, Kouam J, Djebara A. Machining and machinability of aluminum alloys. Alum Alloys Theory Appl 2011:377–400.

[2] Committee AH. Properties and selection: nonferrous alloys and special-purpose materials. ASM International; 1990. https://doi.org/10.31399/asm.hb.v02.9781627081627.

[3] Prime MB, Hill MR. Residual stress, stress relief, and inhomogeneity in aluminum plate. Scr Mater 2002;46(1):77–82.

[4] Chen B, Xi X, Tan C, Song X. Recent progress in laser additive manufacturing of aluminum matrix composites. Curr Opin Chem Eng 2020;28:28–35.

[5] Zhang Z, Zhang Z, Zhang D, Luo M. Milling distortion prediction for thin-walled component based on the average MIRS in specimen machining. The International Journal of Advanced Manufacturing Technology 2020;111(11):3379–92.

[6] Santos MC, Machado AR, Sales WF, Barrozo MA, Ezugwu EO. Machining of aluminum alloys: a review. The International Journal of Advanced Manufacturing Technology 2016;86(9):3067–80.

[7] Guo H, Zuo D, Wu H, Xu F, Tong G. Prediction on milling distortion for aero-multi-frame parts. Materials Science and Engineering: A 2009;499(1–2):230–3.

[8] Chatelain J-F, Lalonde J, Tahan A. A comparison of the distortion of machined parts resulting from residual stresses within workpieces. Proceedings of the 4th International Conference on Manufacturing Engineering, Quality and Production Systems (MEQAPS11). 2011. p. 79–84.

[9] Huang X, Sun J, Li J, Han X, Xiong Q. An experimental investigation of residual stresses in high-speed end milling 7050-t7451 aluminum alloy. Advances in Mechanical Engineering 2013;5:592659.

[10] Richter-Trummer V, Koch D, Witte A, Dos Santos J, De Castro P. Methodology for prediction of distortion of workpieces manufactured by high speed machining based on an accurate through-the-thickness residual stress determination. The International Journal of Advanced Manufacturing Technology 2013;68(9–12):2271–81.

[11] Huang X, Sun J, Li J. Finite element simulation and experimental investigation on the residual stress-related monolithic component deformation. The International Journal of Advanced Manufacturing Technology 2015;77(5–8):1035–41.

[12] Cerutti X, Mocellin K. Influence of the machining sequence on the residual stress redistribution and machining quality: analysis and improvement using numerical simulations. The International Journal of Advanced Manufacturing Technology 2016;83(1–4):489–503.

[13] Becker B. Advanced machining toolpath for low distortion. Tech. Rep. Third Wave Systems, Inc. Eden Prairie United States; 2017.

[14] Ma Y, Zhang J, Yu D, Feng P, Xu C. Modeling of machining distortion for thin-walled components based on the internal stress field evolution. The International Journal of Advanced Manufacturing Technology 2019;103(9):3597–612.

[15] Barcenas L, Ledesma-Orozco E, Van-der Veen S, Reveles-Arredondo F, Rodríguez-Sánchez EA. An optimization of part distortion for a structural aircraft wing rib: an industrial workflow approach. CIRP J Manuf Sci Technol 2020;28:15–23.

[16] Casuso M, Polvorosa R, Veiga F, Suárez A, Lamikiz A. Residual stress and distortion modeling on aeronautical aluminum alloy parts for machining sequence optimization. The International Journal of Advanced Manufacturing Technology 2020;110(5):1219–32.

[17] Fan L, Tian H, Li L, Yang Y, Zhou N, He N. Machining distortion minimization of monolithic aircraft parts based on the energy principle. Metals (Basel) 2020;10(12):1586.

[18] Komanduri R, McGee J, Thompson RA, Covy JP, Truncale FJ, Tipnis VA, et al. On a methodology for establishing the machine tool system requirements for high-Speed/high-Throughput machining. Journal of Engineering for Industry 1985;107(4):316–24. https://doi.org/10.1115/1.3186004.

[19] Sim W-M. Challenges of residual stress and part distortion in the civil airframe industry. Int J Microstruct Mater Prop 2010;5(4–5):446–55.

[20] Wang J, Zhang D, Wu B, Luo M. Prediction of distortion induced by machining residual stresses in thin-walled components. The International Journal of Advanced Manufacturing Technology 2018;95(9):4153–62.

[21] Liu CR, Barash MM. Variables governing patterns of mechanical residual stress in a machined surface. Journal of Engineering for Industry 1982;104(3):257–64. https://doi.org/10.1115/1.3185828.

[22] Smith S, Tlusty J. An overview of modeling and simulation of the milling process. Journal of Engineering for Industry 1991;113(2):169–75. https://doi.org/10.1115/1.2899674.

[23] Ehmann K, Kapoor S, DeVor R, Lazoglu I. Machining process modeling: a review. Journal of Manufacturing Science and Engineering, Transactions of the ASME 1997;119(4B):655–63.

[24] Lukic D, Cep R, Vukman J, Antic A, Djurdjev M, Milosevic M. Multi-criteria selection of the optimal parameters for high-speed machining of aluminum alloy al7075 thin-walled parts. Metals (Basel) 2020;10(12):1570.

[25] Agba EI. Characterization of aluminium rib distortion under high speed machining. i-Manager's Journal on Mechanical Engineering 2011;1(4):20.

[26] Schajer GS. Practical Residual Stress Measurement Methods. John Wiley & Sons; 2013.

[27] Kandil FA, Lord JD, Fry AT, Grant PV. A review of residual stress measurement methods - a guide to technique selection. NPL Report. Teddington: National Physical Laboratory; 2001.

[28] Qian X, Yao Z, Cao Y, Lu J. An inverse approach for constructing residual stress using bem. Eng Anal Bound Elem 2004;28(3):205–11.

[29] Korsunsky A. Eigenstrain analysis of residual strains and stresses. The Journal of Strain Analysis for Engineering Design 2009;44(1):29–43.

[30] Song X, Korsunsky AM. Fully two-dimensional discrete inverse Eigenstrain analysis of residual stresses in a railway rail head. J Appl Mech 2011;78(3).

[31] Farrahi G, Faghidian S, Smith D. An inverse approach to determination of residual stresses induced by shot peening in round bars. Int J Mech Sci 2009;51(9–10):726–31.

[32] Farrahi G, Faghidian S, Smith D. Reconstruction of residual stresses in autofrettaged thick-walled tubes from limited measurements. Int J Press Vessels Pip 2009;86(11):777–84.

[33] Farrahi G, Faghidian S, Smith D. A new analytical approach to reconstruct residual stresses due to turning process. Proceeding of World Academy of Science Engineering and Technology. 55. Citeseer; 2009. p. 453–7.

[34] Farrahi G, Faghidian S, Smith D. An inverse method for reconstruction of the residual stress field in welded plates. J Press Vessel Technol 2010;132(6).

[35] Faghidian SA. A smoothed inverse eigenstrain method for reconstruction of the regularized residual fields. Int J Solids Struct 2014;51(25–26):4427–34.

[36] Do S, Serasli K, Smith D. Combined measurement and finite element analysis to map residual stresses in welded components. Pressure Vessels and Piping Conference. 55713. American Society of Mechanical Engineers; 2013. V06BT06A065

[37] Coules H, Smith D, Venkata KA, Truman C. A method for reconstruction of residual stress fields from measurements made in an incompatible region. Int J Solids Struct 2014;51(10):1980–90.

[38] Chukkan JR, Wu G, Fitzpatrick ME, Jones S, Kelleher J. An iterative technique for the reconstruction of residual stress fields in a butt-welded plate from experimental measurement, and comparison with welding process simulation. Int J Mech Sci 2019;160:421–8.

[39] Chen MJ, Aquino W, Walsh TF, Reu PL, Johnson KL, Rouse JW, et al. A generalized stress inversion approach with application to residual stress estimation. J Appl Mech 2020;87(11):111007.

[40] Sunny S, Mathews R, Gleason G, Malik A, Halley J. Effect of metal additive manufacturing residual stress on post-process machining-induced stress and distortion. Int J Mech Sci 2021;202:106534.

[41] DOD U. Metallic materials and elements for aerospace vehicle structures. United States Department of Defense, Washington, DC MILHDBK-5H 1998.

[42] Johnson GR. A constitutive model and data for materials subjected to large strains, high strain rates, and high temperatures. Proc 7th Inf Sympo Ballistics 1983:541–7.

[43] Sun FL, Sun J, Li JF, Song LY, Luo YG. Accurate measurement of cte of aluminum alloy 7050-t7451 and the impact on thermal deformation analysis. Advanced Materials Research. 566. Trans Tech Publ; 2012. p. 476–9.

[44] Fu XL, Wang H, Wan Y, Wang XQ. Material constitutive model in machining 7050-t7451 by orthogonal machining experiments. Advanced Materials Research. 97. Trans Tech Publ; 2010. p. 713–6.

[45] Liu H, Zhang J, Xu X, Zhao W. Experimental study on fracture mechanism transformation in chip segmentation of ti-6al-4v alloys during high-speed machining. J Mater Process Technol 2018;257:132–40.

[46] Bai Y, Wierzbicki T. A new model of metal plasticity and fracture with pressure and lode dependence. Int J Plast 2008;24(6):1071–96.

[47] Lou Y, Yoon JW, Huh H. Modeling of shear ductile fracture considering a changeable cut-off value for stress triaxiality. Int J Plast 2014;54:56–80.

[48] Cao J, Fuguo L, Xinkai M, Zhankun S. Study of fracture behavior for anisotropic 7050-t7451 high-strength aluminum alloy plate. Int J Mech Sci 2017;128:445–58.

[49] Bal B, Karaveli K, Cetin B, Gumus B. The precise determination of the johnson–cook material and damage model parameters and mechanical properties of an aluminum 7068-t651 alloy. J Eng Mater Technol 2019;141(4).

[50] Hooputra H, Gese H, Dell H, Werner H. A comprehensive failure model for crashworthiness simulation of aluminium extrusions. Int J Crashworthiness 2004;9(5):449–64.

[51] Cao J, Li F, Ma W, Wang K, Ren J, Nie H, et al. A strain rate dependent fracture model of 7050 aluminum alloy. Metals (Basel) 2020;10(1):3.

[52] Chowdhury I, Dasgupta SP. Computation of rayleigh damping coefficients for large systems. The Electronic Journal of Geotechnical Engineering 2003;8(0):1–11.

[53] Rahul B, Dharani J, Balaji R. Optimal method for determination of rayleigh damping coefficients for different materials using modal analysis. Int J Vehicle Structures & Systems 2021;13(1):102–11.

[54] Wang B, Liu Z. Investigations on deformation and fracture behavior of workpiece material during high speed machining of 7050-t7451 aluminum alloy. CIRP J Manuf Sci Technol 2016;14:43–54.

[55] Ravichandran G, Rosakis AJ, Hodowany J, Rosakis P. On the conversion of plastic work into heat during high-strain-rate deformation. AIP Conference Proceedings. 620. American Institute of Physics; 2002. p. 557–62.

[56] Ng E, Szablewski D, Dumitrescu M, Elbestawi M, Sokolowski J. High speed face milling of a aluminium silicon alloy casting. CIRP Ann 2004;53(1):69–72.

[57] Radwan A. Investigation of secondary deformation zone and mean coefficient of friction during the machining of 5083-h34 aluminum alloy. Wear 1985;101(3): 191–204.

[58] Yoshimura H, Moriwaki T, Ohmae N, Nakai T, Shibasaka T, Kinoshita H, et al. Study on near dry machining of aluminum alloys. JSME International Journal Series C Mechanical Systems, Machine Elements and Manufacturing 2006;49(1): 83–9.

[59] Zhang S, Wu Y, Gong H. A modeling of residual stress in stretched aluminum alloy plate. J Mater Process Technol 2012;212(11):2463–73.

[60] Jomaa W, Mechri O, Lévesque J, Songmene V, Bocher P, Gakwaya A. Finite element simulation and analysis of serrated chip formation during high–speed machining of aa7075–t651 alloy. J Manuf Process 2017;26:446–58.

[61] Mabrouki T, Girardin F, Asad M, Rigal J-F. Numerical and experimental study of dry cutting for an aeronautic aluminium alloy (a2024-t351). Int J Mach Tools Manuf 2008;48(11):1187–97.

[62] Dao K, Shockey D. A method for measuring shear-band temperatures. J Appl Phys 1979;50(12):8244–6.

[63] Owen D, Vaz Jr M. Computational techniques applied to high-speed machining under adiabatic strain localization conditions. Comput Methods Appl Mech Eng 1999;171(3–4):445–61.

[64] Thomas M, Turner S, Jackson M. Microstructural damage during high-speed milling of titanium alloys. Scr Mater 2010;62(5):250–3.

[65] Fang N, Yang J, Liu N. Analytical predictive modeling of serrated chip formation in high speed machining of 7075-t6 aluminum alloy. ASME International Mechanical Engineering Congress and Exposition. 47136; 2004. p. 769–77.

[66] Li J-g, Wang S-q. Distortion caused by residual stresses in machining aeronautical aluminum alloy parts: recent advances. The International Journal of Advanced Manufacturing Technology 2017;89(1–4):997–1012.